POLITECNICO DI MILANO

in partial fulfillment of the requirements for the degree of

Doctor in Structural, Earthquake and Geotechnical Engineering

XXIV cycle

Finite element modeling of thermal induced fracture propagation in brittle materials

by

Giovanna Bucci

Accepted by .....
Roberto Paolucci
Doctoral School of Structural, Earthquake and Geotechnical Engineering
Coordinator

March 2012

Acknowledgments

All my gratitude

to Professor Anna Pandolfi for introducing me to the nonlinear solid mechanics and its finite element code implementation

to Progetto Roberto Rocca, for investing in my education and offering me invaluable opportunities in the US

to Professor Raúl Radovitzky, for welcoming me in his research group at MIT, where my curiosity has been encouraged and nourished

to my mentor Professor Carlo Cinquini, for always being a reference and a model

alla mia famiglia, perchè conosce tutta la storia dall'inizio

to Bart, Gail and Greg, for being my American family

to Brandon, for all the rest

Contents

List of Figures

Chapter 1

Introduction

The development of a broad understanding of fracture has embraced the underlying processes determining the deformation and strength of the material as well as the influences of the environment upon them. Researches have been concentrated on studying the microscopic mechanisms which govern fracture and on the establishment, from a macroscopic point of view, of a quantitative fracture criteria for assessing fracture of components.

According to Griffith's theory [15] the quasi-static propagation of a brittle crack is governed by the balance between energy release rate and fracture toughness

$$G = G_c. \tag{1.1}$$

The driving force for crack propagation is the so called energy release rate G, the amount of elastic energy released by the body when the crack itself advances of a unit area. It is function of geometry and load, instead G_c is regarded as a material parameter.

This concept has been the subject of several fundamental works in fracture mechanics among which a couple of landmarks should be cited: the representation of G in terms of the stress intensity factors, due to Irwin [21], and the representation in terms of the J-integral, due to Rice [31]. Through the Irwin formula the interpretation of the fracture propagation criterion may be shifted from the energy based condition

to one based on stress intensity. In perfectly brittle materials we may write

$$K_I = K_{Ic}, \tag{1.2}$$

where the stress intensity factor K_I is expression of the stress concentration at the crack tip under mode I load and the fracture toughness K_{Ic} is a material property. The nucleation or the condition of growing are non sufficient information to describe the fracture process. The path along which a crack propagates when the body is under mixed mode loading is, in fact, generally non-straight. The prediction of the crack path has represented a classical challenge for the fracture mechanics, several are the contributions to the literature, starting from the '60. Among them the *principal of local symmetry* [14], *maximum energy release rate* [5] and the *maximum circumferential stress* [37] are able to predict the angle of deviation of the crack (kinking angle). Classical analytical results on the principal of local symmetry are provided by mean of an asymptotic expansion of the crack path in a small neighborhood of the kinking point. For instance the governing equation of the principle of local symmetry is

$$K_{II} = 0, \tag{1.3}$$

i.e., that the crack always propagates in mode I, so that in-plane tractions that remain perpendicular to the crack in a small neighborhood of the crack tip. These analytical methods are able to detect the instability of the crack respect to the straight propagation within some geometric and loading restrictions. The aim of this research is to give a contribution to the tracking of complex fracture patterns without some of the limitations imposed by analytical formulations and exploiting part of the potential of the numerical treatment of the problem. We focus on brittle fracture propagation in quasi-static condition and in presence of a thermal gradient which represents the driving loading of the crack growth. A transient thermal gradient applied to a conductive body acts as a mixed mode loading and provides less explored conditions for the study of fracture mechanics. At the same time heating and/or cooling may be a reason of damaging and crack nucleation, particularly in thin structures. Our goal is

to develop a finite element model in order to describe the thermo-mechanical process and the fracture phenomenon in thin plates made of brittle materials, such as glass or PMMA.

In a local characterization of the mechanisms of fracture, we conveniently define a fracture cohesive zone. In a small region ahead of the crack tip the separation process is supposed to be active but not complete: the two fracture flanks interact with forces that decrease with the opening displacements, as long as the distance which separate the crack lips does not reach a critical value. The concept of cohesive zone model is due to Dugdale [10] and Barenblatt [1] while an important contribution for its numerical implementation by mean of cohesive finite elements was offered by Camacho-Ortiz [4] and Pandolfi-Ortiz [29] [28]. This technique allows the representation of fracture as a discontinuity in the domain and it may be a powerful tool to follow the crack growth without requiring any a-priori knowledge about its path. One of our main interest is, in fact, to capture the origin of possible instabilities in the fracture direction, in the form of kinking and branching, the appearance of patterns characterized by different level of regularity, symmetry and repetitiveness.

1.1 Inspiring experimental results

The propagation direction of a crack as a function of the external loading and in particular the stability of a straight propagation are fundamental problems of fracture mechanics but not yet fully understood. One of the obstacles to this understanding is represented by the difficulty to perform well-controlled experiments.

Multiple simple tests have showed that a crack travelling in a thin glass plate with a thermal stress field undergoes a reproducible sequence of instabilities. The experiment (sketched in Fig.1-1) is conducted by slowly pulling the sample from a hot region to a cold one, so that in effect a sharp thermal gradient moves across the plate. The plate is seeded with a crack , which the thermal stresses cause to extend at the immersion speed. Since the adopted range of velocities is much slower than the speed of sound in glass, the phenomenon may be regarded as quasi-static. Fracture

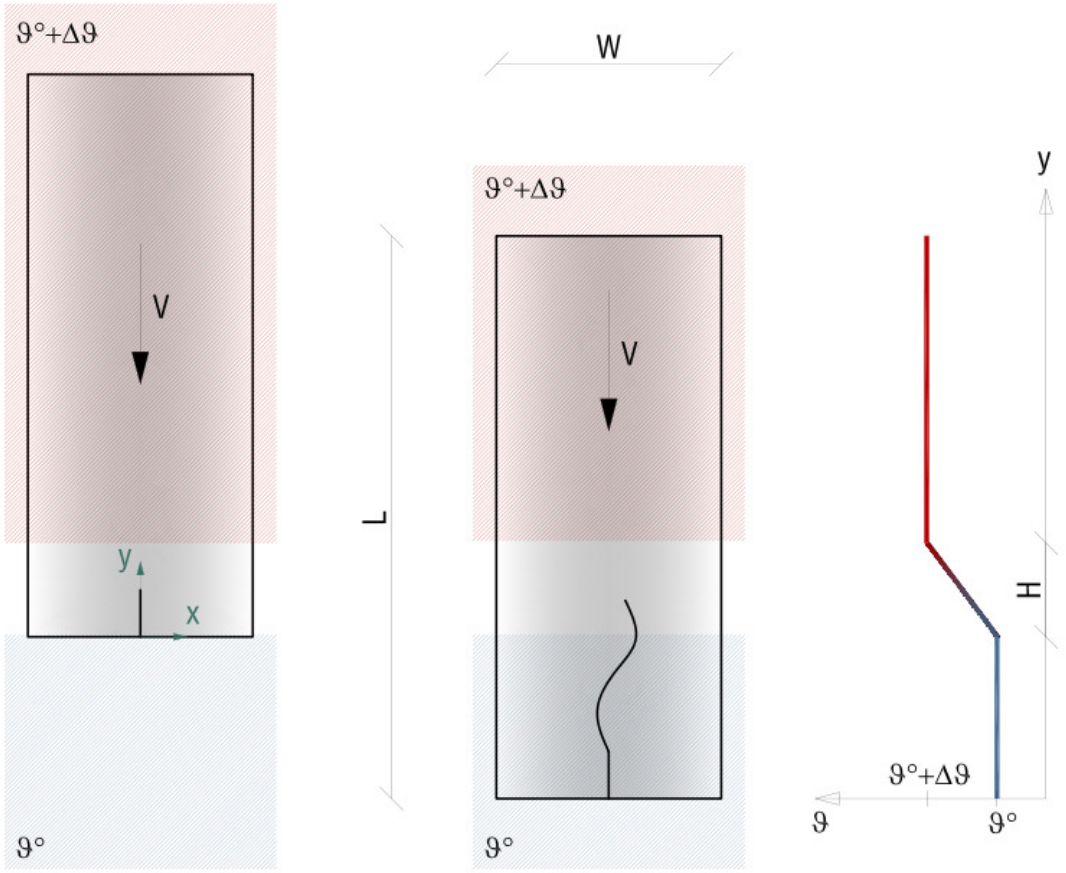

Figure 1-1: Schematic illustration of the set-up for the numerical tests we aim to perform

propagation in the glass plate due to sudden but controlled cooling shows drastic morphological changes depending on the values of the experimental parameters. The patterns observed can be grouped in four categories:

i) no propagation

ii) straight propagation (see Fig.1-2a)

iii) crack oscillating with different possible amplitudes (see Fig.1-2e, Fig.1-2c, Fig.1-2d, Fig1-3a)

iv) branching patterns of various complexity (see Fig.1-3b, Fig.1-3c)

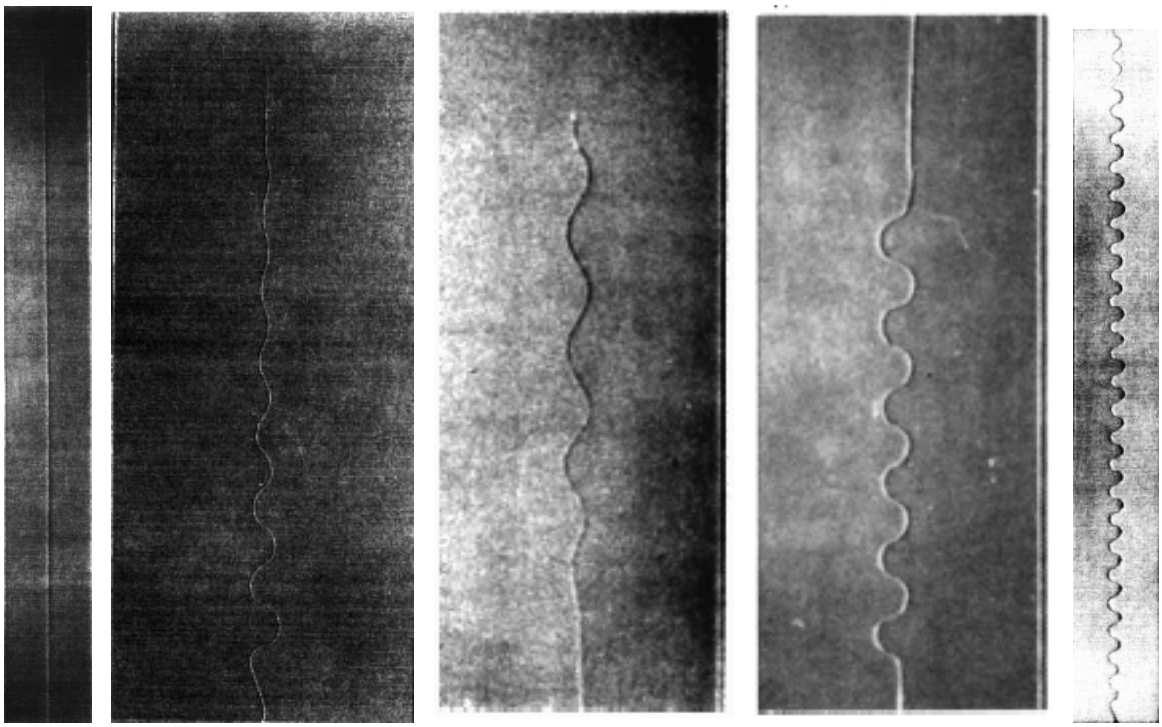

Figure 1-2: Crack patterns recorded in [43], [44]: a) straight propagation; b) dumped oscillating pattern; c) sinusoidal pattern; d) oscillating propagation in a large plate; e) oscillating crack propagating along a narrow plate.

The amorphous nature of glass is supposed to not interfere with the direction of fracture kinking. A similar experimental set, adopted for single-crystal silicon wafers by Deegan et al. [9], has revealed similar instabilities in the fracture development,

even starting from an asymmetric notch and accounting for the relevant anisotropy of the material.

The nucleation of a crack in absence of an initial notch requires in general a severe temperature gradient, so a large value of $\Delta\vartheta$, the temperature difference between hot and cold reservoir. In order to perform experiments with a limited temperature gap and avoid many fractures spontaneously propagating, according to the experimentalists the sample has been equipped with an initial vertical crack in the center of the bottom edge of the plate. The initial crack may perturb the developing pattern but after a transient the effect tends to disappear re-establishing the conditions due to the control parameters. If the orientation of the notch is inclined respect to the vertical axis, the propagation shows an initial oscillation dumped to a straight line (see Fig.1-2b), when the experiment is performed within the range of straight crack conditions.

Each couple of values ($\Delta\vartheta$, V), where V is the immersion velocity, provides the system with a certain amount of internal energy available for fracturing the material. The thermal gradient and the imposed velocity need to be severe enough to drive the propagation of the crack. During growth the crack may select different patterns, to dissipate different quantities of energy by creating of new surfaces. Increasing the value of $\Delta\vartheta$, for a fixed driving velocity, it is possible to observe the transition from straight to periodic oscillating propagation and finally to the branched one, in the sense of a progressive extension of the total fracture area.

The wavelength and the amplitude characterizing the oscillation in the fracture profiles depend on the control parameters. When the velocity is slightly beyond the onset of oscillation, the crack shape is almost sinusoidal (see Fig.1-2c). As V or $\Delta\vartheta$ is increased, the shape becomes a sequence of semicircles (see Fig.1-2d) and finally becomes asymmetric in the direction of propagation (see Fig.1-3a). Oscillations of branched cracks could be irregular, their amplitude modulated or chaotic. The number of branches varies with the driving parameters, different levels of complexity and disorder have been observed. Yuse and Sano [43], [44] investigated the role of the descent velocity V and of the temperature gap between the initial plate temperature

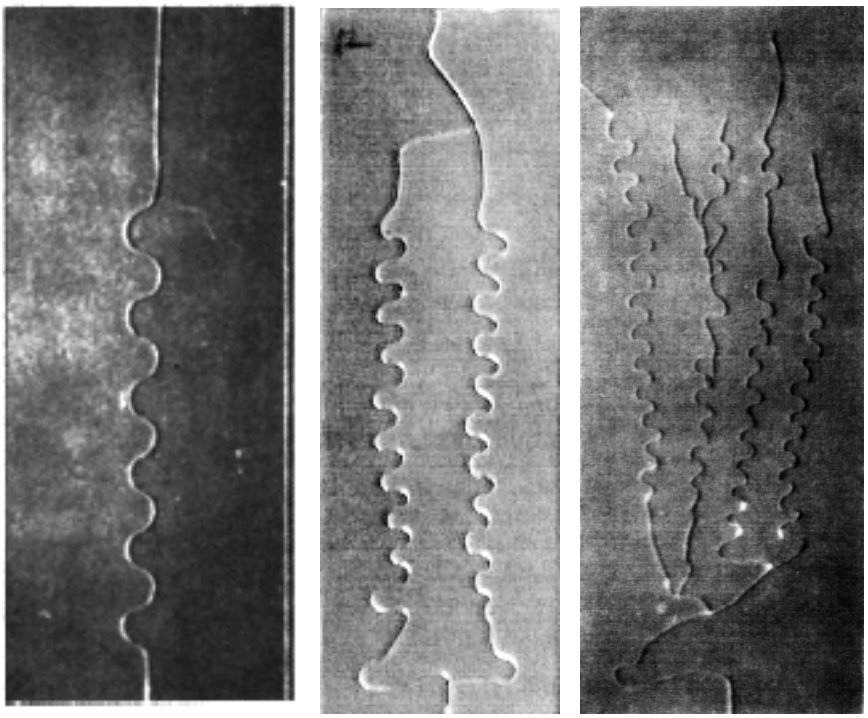

(a) oscillating crack pattern describing semicircles

(b) two-branch crack with oscillation

(c) pattern with multiple branches

Figure 1-3: Instable crack patterns documented in [43], [44]

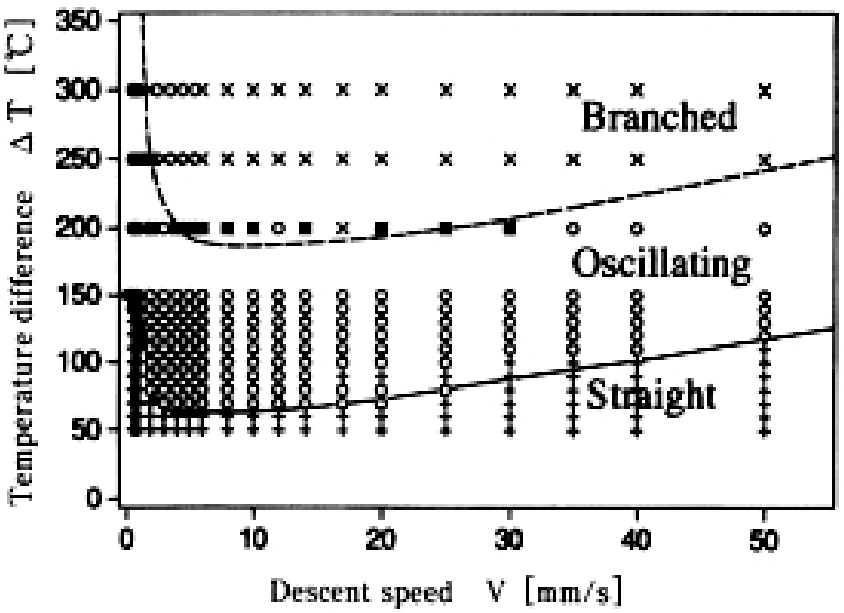

Figure 1-4: The data resulting from the experiments on glass plates (of dimensions 24 x 60 x 0.13 mm^3 carried out by Yuse and Sano have been grouped in a phase diagram in relation to the values of immersion velocity and temperature gap.

and the cold reservoir $\Delta\vartheta$, provided by a water bath.

The upper dashed line in 1-4 denotes the threshold for the appearance for branched cracks, with some dispersion. The lower solid line represents the boundary between the oscillating pattern and the straight one. Threshold lines have negative slope for $V < 10\mathrm{mms}^{-1}$ and positive slope for $V > 10\mathrm{mms}^{-1}$. This result has been interpreted by the authors as due to the cooling delay of the last portion of the plate immersed into the water (heat transient regime) and to a non isothermal condition across the sample thickness. The thickness of the plate related to the thermal diffusion length

$$d_{th} = \frac{\kappa}{V}, \tag{1.4}$$

with κ being the glass thermal diffusion coefficient

$$\kappa = \frac{k}{\varrho C_v} \tag{1.5}$$

determines, in fact, the passage from a two- to a three-dimensional processes.

In their study Ronsin, Heslot and Perrin [32], [33], [34] introduced a third parameter represented by the plate width W and they focused on the influence of the geometry of the plate on the propagation of a single or multiple cracks. For a given thermal field the internal energy stored in the glass plate depends on specimen width. The quantity of energy accumulated into the material is released to feed the fracture advance and to influence the crack pattern. The set of Fig.1-5 illustrates, for a given thermal field ($\Delta\vartheta$, the spatial gap between hot and cold region H, V fixed), the crack growth state dependent on the plate width in relation to some critical values which represent the transition from no crack development to the straight propagation and eventually to the oscillating one (see Fig. 1-5). It is also interesting to observe the progressive destabilization of the pattern respect to the symmetric straight line in a sample with increasing width (Fig. 1-6). These experimental results are recalled in more detail in the section 4.2.3 with the purpose of analysing and comparing our numerical outcomes.

1.2 Subject overview

A straight crack propagating in the middle of the plate is, according to the symmetries, a pure mode I fracture problem. Crack initiation observations reveal that the presence of shear stress at the crack tip leads to a direction of growth making a finite angle with the initial crack direction. This suggests that smooth propagation occurs along a path where the condition for the crack tip is given by

$$K_{II} = 0. \tag{1.6}$$

This is usually referred to as *the criterion of local symmetry* [14]. Applying this concept, Cotterel and Rice [6] have demonstrated that for a crack growing in an infinite plate, the stability of the straight direction is due to the non-singular longitudinal tensile stress T at the crack tip. In presence of a positive value of T, the fracture deviates from the initial trajectory of motion, instead if T is negative the crack stably

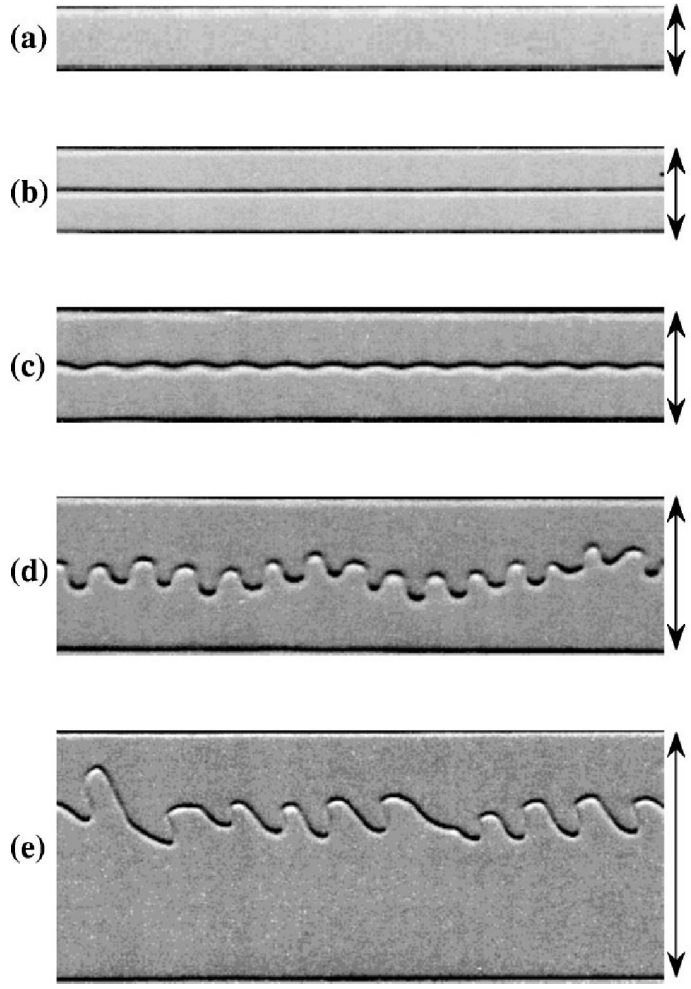

Figure 1-5: Three states are observed according to the sample width W: a) no propagation for $W < W_c$; b)straight propagation for $W_c < W < W_{osc}$; c)oscillating propagation for $W > W_{osc}$; e),d)non-regular oscillation for $W >> W_{osc}$

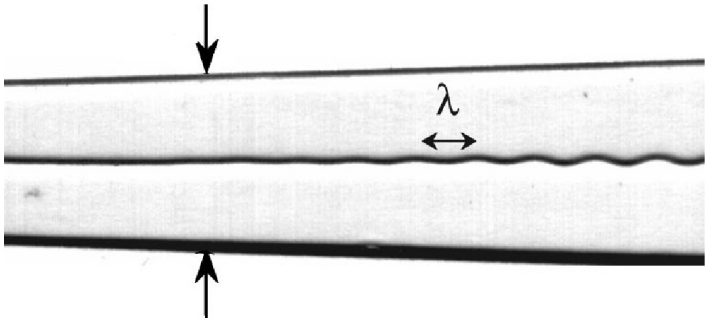

Figure 1-6: Glass plate characterized by increasing width. The sample has been used by [34] to estimate the critical value W_{osc}, which corresponds to the de-stabilization of the straight crack.

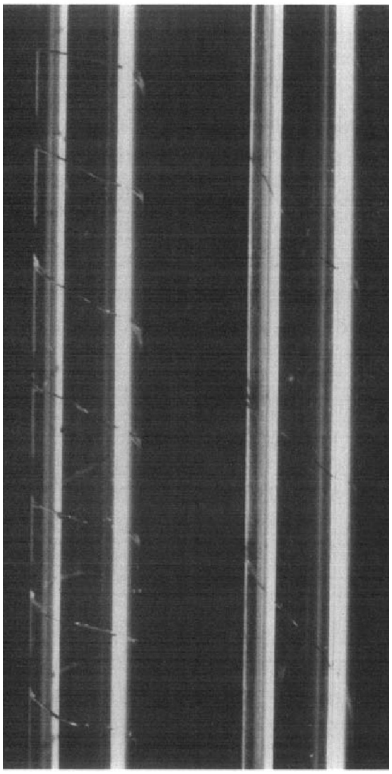

Figure 1-7: Helical cracks in cylindrical samples quenched in cold water. Experiment recorded in [44] to underline the effect of different boundary conditions on the crack path.

propagates following a straight path. The limit of the application of Cotterel and Rice condition is related to the sample width W: to determine when the infinite plate approximation might be appropriate, the dimension W needs to be compared to the thermal diffusion length. The restriction to large enough values of W and V may be considered as a limit of the criterion. Furthermore, the boundary conditions represented by the free lateral edges of the plate are necessary for the oscillation as well as the instability phenomenon which first deviates the crack form the straight propagation. The boundary allows the relaxation of the stress near the edges and induces a restoring force towards the center, where the tensile stress due to the thermal contraction is larger. As a matter of fact, in cylindrical samples no change of direction has been observed (Fig.1-7) the crack propagates with a fix angle following an helical pattern whose pitch depends on the experimental parameters.

The transition from a straight to an oscillatory propagation has been interpreted

in literature through the Cotterel and Rice criterion by Marder [23] as well as a Hopf bifurcation by Sasa et al. [36], in both cases referring to infinite plate approximation. When a problem depends on some parameters (like V, $\Delta\vartheta$ and W), the solution space may represented by a non-smooth manifold and the appearance of the stable closed orbits is interpreted as a "shift of stability" from the original stationary solution to the periodic one [24], [16]. This approach reveals the potential of capturing from a general point of view the crack behaviour, according to the imposed external conditions. The mathematical concept is explained and illustrated with an example at the section 4.4.

From the numerical point of view, a few references are available in the literature. Among them, we cite a couple of attempts to simulate the experimental results described in the preceding paragraph. By adopting a peridynamic theory Kilic et al. in [22] reproduce complex crack patterns by mean of a damage model. The technique has the limit of not allowing the use of a generic Poisson coefficient (it is constraint to 0.25 by the general assumptions of the theory). Furthermore, like other damage models, it is able to describe a local reduction of the stiffness of the material but not to explicitly model the fracture as a discontinuity produced in the solid. In order to obtain meaningful results the authors needed to assign a slope to initial notch and apply values of $\Delta\vartheta$ and in particular of V much higher than the experimental ones. In [11] Ferney et al. document some examples of oscillating and branched cracks modelled by cohesive finite element. The simulation does not follow the experimental condition: the expedient of increasing the descent speed (of six orders of magnitude) changes the process from quasi-static to dynamic.

1.3 Analysis and modeling of the problem

1.3.1 Dimensional analysis

The number of numerical analysis that we are able to perform is limited by the computational cost of each of them; at the same time we want to be able to compare the numerical results with the large number of experimental data available in literature.

A possible way is to perform a dimensional analysis and use dimensionless parameters to characterize the system and represent the outcomes.

The geometry of the problem is described by the following dimensionless parameters (being D the thickness of the plate):

i) $\frac{D}{L}$ (D tends to be very small compared to its length).

ii) $\frac{W}{L}$ (the ratio between the two relevant dimensions of the plate);

iii) $\frac{H}{L}$ (the spatial gap between hot and cold regions respect to the total sample length).

The heat problem is essentially governed by the Biot and the Peclet numbers

iv) $Bi = \frac{hD/2}{k}$ (which describes the conduction problems that involve surface convection effects),

v) $Pe = \frac{HV}{\kappa}$ (which the ratio of the rate of advection of a physical quantity by the flow to the rate of diffusion of the same quantity driven by an appropriate gradient. In the context of the transport of heat, the Peclet number is equivalent to the product of the Reynolds number and the Prandtl number).

In the definitions h is the convection heat transfer coefficient, k is the thermal conductivity and κ the thermal diffusion coefficient.

This two values are very relevant in understanding the interaction between therma and mechanical problem. More detailed considerations will follow in the next two sections.

To summarize the information about the fracture traveling along the specimen, we will make use of the following dimensionless quantities:

vi) $t_{nm} = \frac{Vt}{L}$ (the dimensionless time);

vii) $arel = \frac{a}{L}$ (the fracture length divided by the plate length);

viii) $\dot{a}_{rel} = \frac{\dot{a}}{V}$ (the fracture propagation velocity compared to the immersion one).

The quantities concerning the thermo-mechanical problem may be classified as follow

ix) ν (the Poisson coefficient);

x) $\alpha\Delta\vartheta$ (which characterize the thermal volumetric deformation);

xi) $\dfrac{VE}{h\Delta\vartheta}$;

xii) $\dfrac{VG_c}{Wh\Delta\vartheta}$.

The last two parameter may be combined to formulate quantities that are more meaningful, for capturing and communicating the results of our numerical studies.

A natural choice for one of them is represented by the ratio between an increment of the elastic energy and the fracture energy necessary for a straight extension of the crack surface. We may compute the variation of the strain energy per unit of plate thickness

$$\delta E_{strain} = E\alpha^2\Delta\vartheta^2 W \tag{1.7}$$

and compare it with the amount of energy released for propagating the fracture, obtaining the dimensionless parameter τ

$$\tau = \frac{E(\alpha\Delta\vartheta)^2 W}{G_c}. \tag{1.8}$$

The temperature gradient and the plate width may be chosen in order to keep the same value of τ: in this way experimental as well as numerical results carried out on a range of descent speed values are equivalent to a set of tests, conducted varying the sample width. In our application we assume constant material properties: Young modulus $E = 70$ GPa, the coefficient of linear expansion $\alpha = 9\cdot 10^{-6}\mathrm{K}^{-1}$, the thermal diffusion coefficient $\kappa = 0.47\mathrm{mm}^2\mathrm{s}^{-1}$. In the literature ([32], [23], ...) the value of the fracture energy has been analyzed as function of the temperature at the crack tip and of the driving velocity. It is beyond the purpose of this work to consider the dependence of the fracture energy on other parameters, so we will consider a constant average value.

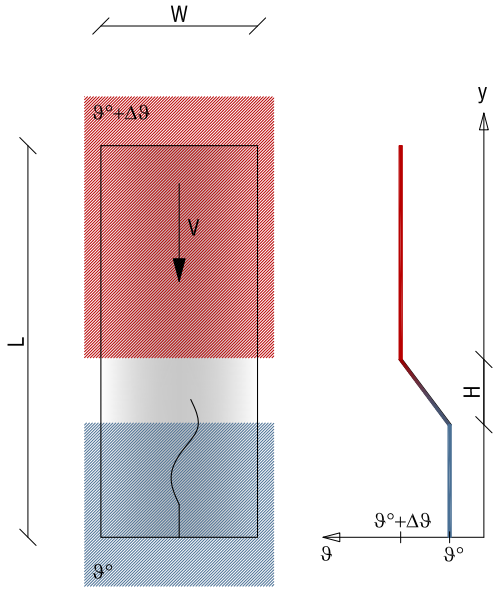

Figure 1-8: Geometry of the experimental setup.

The rate of the energy released by the propagating fracture may be compared to the convective flux coming form the plate surfaces immersed into the water. The definition of the relative dimensionless parameter may be the following

$$\zeta = \frac{G_c \dot{a}}{hW\Delta\vartheta}. \tag{1.9}$$

The geometry of the palate considered in the numerical computations is described by the following constant quantities (see Fig.1-8)

$L = 60$ mm (plate length);

$W = 20$ mm (plate width);

$H = 20$ mm (distance between the water bath and the heated region of the plate).

1.3.2 Two-dimensional modelling of the heat problem

The adoption of a two-dimensional model may simplify the analysis and reduce the computational cost of the simulations.

This approximation may be justified by verifying the Biot number. It provides a measure of the temperature drop in the solid relative to the temperature difference between the surface and the fluid [2] [20]. The resistance to conduction within the solid is much lower than the resistance to convection across the fluid boundary layer if

$$Bi \ll 1. \tag{1.10}$$

In this case it is reasonable to assume a uniform temperature distribution within the solid at any time during a transient process. The quantity to be verified is

$$Bi = \frac{h}{k}, \tag{1.11}$$

where h is the convection heat transfer coefficient, k is the thermal conductivity and L_c is the characteristic length of the heat problem involving conduction and convection. It corresponds to one half of the thickness of the plate for the specific geometry of our problem (plane vertical wall). The data for the quenched plate are:

$$h \sim 10_1 \quad \mathrm{W/m^2K} \tag{1.12}$$

$$k = 0.65 \quad \mathrm{W/m\ K} \tag{1.13}$$

$$L_c = 0.5 \cdot 10^{-4} \quad \mathrm{m} \tag{1.14}$$

$$Bi \sim 10^{-3} < 0.1 \tag{1.15}$$

The order of magnitude of the Biot number allows the assumption of a constant temperature field within the thickness of the plate.

1.3.3 Steady thermal profile

In the problem at the hand, the thermal profile along the plate is related to the temperature difference $\Delta\vartheta$ and the spatial gap H between the two reservoir of the plate: the first is kept at a constant higher temperature T_h, the second is immersed into the the water at temperature T_c. A steady state can be characterized by two constant temperature fields connected by a linear profile along the separation gap. The driving velocity V localizes the thermal gradient in proximity the cold bath over an area measured by the thermal diffusion length. The steady thermal regime may be verified comparing the spatial gap with the thermal diffusion length, obtaining a condition over the immersion velocity, which needs to be low enough to allow the assumption of quasi-static condition. We can verify weather the Peclet number is much lower than the unity or equivalently

$$H \ll \frac{\kappa}{V} \quad \Rightarrow \quad V \ll \frac{\kappa}{H} \tag{1.16}$$

$$\mathrm{V} \ll \frac{0.47\mathrm{mms}^{-1}}{10\,\mathrm{mm}} = 0.047\,\mathrm{mms}^{-1} \tag{1.17}$$

We limited the range of velocities of our simulations, adopting $0.01\,\mathrm{mms}^{-1}$ as maximum value in order to reasonably assume a steady temperature profile and reduce the computational cost of the analysis. In the experiments of Yuse and Sano the velocity reaches the value of $50\,\mathrm{mms}^{-1}$ and manifest crack patterns more and more regular with the increasing of the descent velocity. This apparent antithetical behaviour is due to the increasing complexity of the thermo-mechanical problem, according with two main possible conditions:

- $\frac{\kappa}{h} < V < \frac{\kappa}{D}$ the heat conduction is no longer in steady regime and the temperature gradient localizes near the cold bath over the extent of d_{th}
- $V > \frac{\kappa}{D}$ the thermal diffusion length becomes smaller than the thickness of the plate: the temperature is no longer constant across the thickness, the fracture process becomes three-dimensional and the resulting crack surface is rough.

The localization of the temperature gradient in the proximity the cold bath may

be obtained increasing the driving velocity as well as the distance between the two reservoirs. Aiming to approximate a steady thermal regime, it is possible to perform slower plate immersions or to reduce the area of the diffusion, tuning the H parameter As already observed by [34].

The assumption of a steady thermal regime with perfect thermal baths and a constant temperature gradient in the H region produces a discontinuous temperature gradient field, leading to an overestimate of the stress field concentration at the crack tip interface. The consequence could be a non precise prediction of the crack tip position, influenced anyway by numerical constraints coming from the discretization of the domain.

1.3.4 Organization of the contents

This research has been developed with the intention to solve the thermo-mechanical problem through a finite element code, in a two-dimensional approximation of the spatial set and imposing a steady temperature profile. The fracture propagation in brittle materials has been modeled explicitly with cohesive finite elements in order to predict the crack pattern on the basis of the stress concentration at the crack tip. The instability of the straight crack propagation is derived as an outcome of the numerical analysis, not requiring the formulation of an analytical kinking criterion. This allowed us to avoid the necessity of severe simplification of the problem, such as the hypothesis of infinite plate width that remove the possibility to capture the dependency of the crack path on this geometric parameter.

The contents are organized according to the following subject subdivision. The second chapter describes the general formulation of the thermodynamic problem. The third chapter deals with the spatial discretization and the numerical tools adopted to solve the thermo-mechanical problem and to track the evolution of the crack path. The fourth chapter collects the most relevant results of numerical simulation of the described experiments. Criticality and open issues arising from the analysis are pointed out. The fifth chapter introduce current developments of this research and possible future extension in the problem treatment.

Chapter 2

Non-linear Solid Mechanics

2.1 Thermodynamics of non-linear elastic materials

2.1.1 Introduction

The continuum mechanics (Truesdell and Noll [40], Gurtin et al. [17], Holzapfel [18]) is based on physical entities with a mathematical description. It is essential to consider the concepts of body, regarded as a smooth manifold of material points; configuration of a body, namely a mapping of the body in a three-dimensional Euclidean space; force system acting on a body, defined by a vector-valued function. As constitutive assumptions, force systems may include body forces with a mass density and contact forces, based on a surface density and local properties of the configuration at the point. The thermodynamics of continua includes the concepts of temperature, specific internal energy, specific entropy, heat flux, and heat supply (due to radiation). As general principles of mechanics we take into account the objectivity and the law of balance of linear momentum; we add the fist law of thermodynamics (the law of balance of energy) and the second law of thermodynamics in the form of the Clausius-Duhem inequality. The constitutive assumptions for the material and the purposes of this study are the following:

1. the specific internal energy is a function of the deformation gradient and of the specific entropy;

2. the temperature is related to the deformation gradient and the internal entropy;

3. the stress tensor describes an elastic behavior based on the deformation and the internal entropy, disregarding plastic and viscous effects;

4. the heat flux only depends on the deformation, the specific entropy and the spatial gradient of the temperature.

Necessary and sufficient restrictions are derived imposing the Clausius-Duhem inequality valid for all the admissible processes.

2.1.2 Thermodynamic processes

A thermodynamic smooth process is a time-dependent set of configurations, force systems, temperature, internal energy, entropy, heat supply and heat flux compatible with the principles of mechanics and the law of conservation of energy. A thermodynamic process is admissible when it is compatible with the constitutive assumptions under consideration. Consider a body consisting of material points. It undergoes a thermodynamic process described by eight function of the position $\mathbf{X} \in B \subset \mathbb{R}^2$ of the material point along the time $t \in (0, T) \in \mathbb{R}_+$:

1. the spatial position $\mathbf{x} = \boldsymbol{\chi}(\mathbf{X}, t)$, where $\boldsymbol{\chi}$ is the motion of the body and it is also called configuration mapping;

2. the body force $\mathbf{B} = \mathbf{B}(\mathbf{X}, t)$ per unit of mass;

3. the first Piola Kichhoff stress tensor $\mathbf{P} = \mathbf{P}(\mathbf{X}, t)$;

4. the internal energy density $\varepsilon = \varepsilon(\mathbf{X}, t)$;

5. the heat flux vector $\mathbf{Q} = \mathbf{Q}(\mathbf{X}, t)$,

6. the heat supply $R = R(\mathbf{X}, t)$ per unit of mass and unit of time

7. the specific entropy $\eta = \eta(\mathbf{X}, t)$

8. the local temperature $\vartheta = \vartheta(\mathbf{X}, t)$ assumed to be always positive

When associated to a thermodynamic process the eight functions must satisfy the four conservation laws applied to the whole body and to any sub-part Ω:

1. the law of balance of mass

$$\frac{D}{Dt}\int_{\Omega} \rho(\mathbf{X}, t)\, dV = 0 \tag{2.1}$$

2. the law of balance of linear momentum

$$\int_{\Omega} \rho_0 \ddot{\boldsymbol{\chi}}\, dV = \int_{\Omega} \rho_0 \mathbf{B}\, dV + \int_{\partial\Omega} \mathbf{P}\mathbf{N}\, dS \tag{2.2}$$

3. the law of balance of angular momentum

$$\int_{\Omega} \boldsymbol{\chi} \times \rho_0 \ddot{\boldsymbol{\chi}}\, dV = \int_{\Omega} \boldsymbol{\chi} \times \rho_0 \mathbf{B}\, dV + \int_{\partial\Omega} \boldsymbol{\chi} \times \mathbf{P}\mathbf{N}\, dS \tag{2.3}$$

4. the law of balance of energy

$$\frac{D}{Dt}\int_{\Omega} \left(\frac{1}{2}\rho_0 \dot{\boldsymbol{\chi}}^2 + \varepsilon\right)\, dV = \int_{\Omega} \left(\mathbf{B}\dot{\boldsymbol{\chi}} + R\right)\, dV + \int_{\partial\Omega} \left(\mathbf{P}\dot{\boldsymbol{\chi}} - \mathbf{Q}\right) \mathbf{N}\, dS \tag{2.4}$$

In (2.2), (2.3) and (2.4), dV represents the element of volume of the body in the reference configuration, ∂B the boundary of B, dS the element of surface in the configuration at the reference time, the vector $\mathbf{N}$ the normal to the surface dS, the superimposed dots denote the time-derivatives. In the preceding equations we made use of ρ_0 and ρ to denote the mass per unit of volume computed in the material and spatial configuration respectively.

In the notation we adopt Greek and capital Latin symbols to refer to the undeformed configuration of the body, the so called material or Lagrangian reference. Lower Latin case refers to the spatial or deformed configuration, with the exception of cases when clarity suggests a different choice.

Under suitable compatibility assumptions (the presence of discontinuities due fracture is taken into account and discussed in the next sections) the three balance integral equations (2.2), (2.3) and (2.4) may be formulated locally in differential form:

$$\operatorname{Div}\mathbf{P} + \rho_0\mathbf{B} = \rho_0\ddot{\boldsymbol{\chi}} \tag{2.5}$$

$$\mathbf{P}\mathbf{F}^{\mathbf{T}} = \mathbf{F}\mathbf{P}^{\mathbf{T}} \tag{2.6}$$

$$\dot{\varepsilon} = \mathbf{P} : \dot{\mathbf{F}} - \operatorname{Div}\mathbf{Q} + \rho_0 R \tag{2.7}$$

where $\dot{\mathbf{F}}$ denotes the time derivative of the deformation gradient $\mathbf{F}$, defined as follow:

$$\mathbf{F}(\mathbf{X}, t) = \frac{\partial \boldsymbol{\chi}(\mathbf{X}, t)}{\partial \mathbf{X}} = \operatorname{Grad}\mathbf{x}(\mathbf{X}, t) \qquad \in GL_+(3, \mathbb{R}) \tag{2.8}$$

where $GL_+(3, \mathbb{R})$ is the Lie group of invertible and orientation preserving linear transformations in $\mathbb{R}^3$. It is sufficient to prescribe the six functions $\boldsymbol{\chi}, \mathbf{P}, \varepsilon, \mathbf{Q}, \eta, \vartheta$ to define a thermodynamic process and to uniquely determine $\mathbf{B}, R$.

2.1.3 Constitutive equations

The constitutive assumptions define specific material properties for the body, according with the application under consideration. An elastic material with heat conduction is defined by four response functions:

$$\varepsilon = \varepsilon(\mathbf{F}, \eta) \tag{2.9}$$

$$\vartheta = \vartheta(\mathbf{F}, \eta) \tag{2.10}$$

$$\mathbf{P} = \mathbf{P}(\mathbf{F}, \eta) \tag{2.11}$$

$$\mathbf{Q} = \mathbf{Q}(\mathbf{F}, \eta, \operatorname{Grad}\vartheta) \tag{2.12}$$

Admissible processes are identified by prescribing a mapping $\boldsymbol{\chi}(\mathbf{X}, t)$ and an entropy distribution $\eta(\mathbf{X}, t)$. The deformation gradient is computed from $\boldsymbol{\chi}$ and $\varepsilon, \vartheta, \mathbf{P}, \mathbf{Q}$ can be determined through constitutive laws. It follows that the value of $\mathbf{B}, R$ can be chosen so that the balance equations hold. The principle of material frame indifference

(or objectivity) states that the admissibility of a process must not be affected by a change of frame or observer. According to this principle the constitutive assumptions must result to be indifferent to a change of frame, for example by defining the functions in terms of the right Cauchy-Green tensor $\mathbf{C} = \mathbf{F}^{\mathbf{T}}\mathbf{F}$

$$\varepsilon = \varepsilon(\mathbf{C}, \eta) \tag{2.13}$$

$$\vartheta = \vartheta(\mathbf{C}, \eta) \tag{2.14}$$

$$\mathbf{P} = \mathbf{P}(\mathbf{C}, \eta) \tag{2.15}$$

$$\mathbf{Q} = \mathbf{Q}(\mathbf{C}, \eta, \operatorname{Grad}\vartheta) \tag{2.16}$$

$$\tag{2.17}$$

2.1.4 Entropy inequality principle

The second law of thermodynamics postulates that the total production of entropy is always non negative. Regarding $\mathbf{Q}/\vartheta$ as a flux of entropy and $\rho_0 R/\vartheta$ as a supply of entropy, the second law of thermodynamics takes the form of the Clausius-Duhem inequality:

$$\Gamma(t) = \frac{D}{Dt}\int_\Omega \eta \, dV + \int_{\partial\Omega} \frac{\mathbf{Q}}{\vartheta} \cdot \mathbf{N} \, dS - \int_\Omega \frac{R}{\vartheta} \, dV \geq 0 \tag{2.18}$$

The specific production of entropy is represented by the differential form:

$$\dot{\eta} - \rho_0 \frac{R}{\vartheta} + \frac{1}{\vartheta} \operatorname{Div}\mathbf{Q} - \frac{1}{\vartheta^2}\mathbf{Q} \operatorname{Grad}\vartheta \geq 0 \tag{2.19}$$

An alternative local form is derived by substituting the energy balance into the equation

$$\mathbf{P} : \dot{\mathbf{F}} - \dot{\varepsilon} + \vartheta\dot{\eta} - \frac{1}{\vartheta}\mathbf{Q} \operatorname{Grad}\vartheta \geq 0 \tag{2.20}$$

where the last term represents the entropy production due to heat conduction. The chain rule applied to the internal energy rate reads

$$\dot{\varepsilon} = \frac{\partial\varepsilon}{\partial\mathbf{F}} : \dot{\mathbf{F}} + \frac{\partial\varepsilon}{\partial\eta} : \dot{\eta} \tag{2.21}$$

Let us consider a precess defined by homogeneus deformations and entropy ditribution. Thus $\mathbf{F}, \eta$ may be chosen to be arbitrary functions of time and $\operatorname{Grad}\mathbf{Q} = \mathbf{0}$. The Clausius-Duhem inequality becomes:

$$\left[\vartheta(\mathbf{F},\eta) - \frac{\partial\varepsilon}{\partial\eta}(\mathbf{F},\eta)\right]\dot{\eta} + \left[\mathbf{P}(\mathbf{F},\eta) - \frac{\partial\varepsilon}{\partial\mathbf{F}}\right] : \dot{\mathbf{F}} \geq 0 \tag{2.22}$$

and in order to hold for any homogeneus process we must have

$$\vartheta = \vartheta(\mathbf{F},\eta) = \frac{\partial\varepsilon}{\partial\eta} \tag{2.23}$$

$$\mathbf{P} = \mathbf{P}(\mathbf{F},\eta) = \frac{\partial\varepsilon}{\partial\mathbf{F}}. \tag{2.24}$$

The temperature and stress relations (2.23), (2.24) and the heat conduction inequality

$$-\mathbf{Q}\operatorname{Grad}\vartheta \geq 0 \tag{2.25}$$

may be regarded as sufficient conditions for the validity of the Clausius-Duhem inequality, when applied to any admissible thermoelastic processes. Inequality (2.25) states that the propagation of the heat flux is in the direction of a negative temperature gradient and it states the non-existence of a piezo-caloric effect, namely the absence of heat-conduction in case of a constant temperature field. The temperature relation can be inverted whenever ε is a convex function of η for a fixed $\mathbf{F}$, so that eq. (2.23) can be solved for the entropy

$$\eta = \eta(\mathbf{F},\vartheta) \tag{2.26}$$

Introducing the Helmholtz free energy through the Legendre transformation

$$\psi(\mathbf{F},\vartheta) = \inf_{\eta}\{\varepsilon(\mathbf{F},\eta) - \vartheta\eta\} \tag{2.27}$$

we derive an alternative form for the equations (2.23), (2.24)

$$\eta = \eta(\mathbf{F}, \vartheta) = -\frac{\partial \psi}{\partial \vartheta} \tag{2.28}$$

$$\mathbf{P} = \mathbf{P}(\mathbf{F}, \eta) = \frac{\partial \psi}{\partial \mathbf{F}}. \tag{2.29}$$

The constitutive equations (2.24), (2.23) can be formulated taking into account the material frame indifference, so that the second Piola-Kirchhoff stress tensor and the entropy are defined through the free energy in the form:

$$\mathbf{S}(\mathbf{C}, \vartheta) = 2\frac{\psi(\mathbf{C}, \vartheta)}{\partial \mathbf{C}} \tag{2.30}$$

$$\eta(\mathbf{C}, \vartheta) = -\frac{\psi(\mathbf{C}, \vartheta)}{\partial \vartheta} \tag{2.31}$$

depending only on $\mathbf{C}$ and ϑ.

2.1.5 Thermoelastic field equations

The energy balance can be formulated in terms of entropy in order to obtain a more suitable equation for the statement of the thermoelastic problem. By introducing the Gibbs relations

$$\dot{\psi} = \frac{1}{2}\mathbf{S} : \dot{\mathbf{C}} - \eta\dot{\vartheta} \tag{2.32}$$

$$\dot{\varepsilon} = \frac{1}{2}\mathbf{S} : \dot{\mathbf{C}} + \vartheta\dot{\eta} \tag{2.33}$$

derived from the thermodynamic restrictions considered above, it is possible to substitute the energy balance with the entropy balance

$$\dot{\eta} = -\frac{1}{\vartheta}\operatorname{Div}\mathbf{Q} + \rho_0\frac{R}{\vartheta} \tag{2.34}$$

The expression of the entropy production for a thermo-mechanical process becomes

$$\Gamma = -\frac{1}{\vartheta}\mathbf{Q}(\mathbf{C}, \vartheta, \operatorname{Grad}\vartheta)\operatorname{Grad}\vartheta \tag{2.35}$$

The stress-temperature modulus

$$\mathbf{M}(\mathbf{C},\vartheta) = \frac{\partial \mathbf{S}(\mathbf{C},\vartheta)}{\partial \vartheta} \tag{2.36}$$

is defined as the tensor that measures the change in stress due to a change in temperature (at fixed strain) and the heat capacity (at fixed strain) C_v, defined as the specific heat per unit of mass

$$\rho_0 C_v(\mathbf{C},\vartheta) = \frac{\partial \varepsilon(\mathbf{C},\vartheta)}{\partial \vartheta} = -\vartheta \frac{\partial^2 \psi(\mathbf{C},\vartheta)}{\partial \vartheta^2} \tag{2.37}$$

Differentiating the entropy with respect to the time we get

$$\vartheta \dot{\eta} = \vartheta \frac{\partial \eta(\mathbf{C},\vartheta)}{\partial \mathbf{C}} : \dot{\mathbf{C}} + \vartheta \frac{\partial \eta(\mathbf{C},\vartheta)}{\partial \vartheta} \dot{\vartheta} \tag{2.38}$$

$$= -\frac{1}{2}\vartheta \mathbf{M}(\mathbf{C},\vartheta) : \dot{\mathbf{C}} + c(\mathbf{C},\vartheta)\dot{\vartheta} \tag{2.39}$$

Accounting for the frame indifference and the respect of the thermodynamic principles, the evolution equation for the temperature can be written as follow

$$\rho_0 C_v(\mathbf{C},\vartheta)\dot{\vartheta} = -\operatorname{Div} \mathbf{Q}(\mathbf{C},\vartheta,\operatorname{Grad}\vartheta) + \frac{1}{2}\vartheta \mathbf{M}(\mathbf{C},\vartheta) : \dot{\mathbf{C}} + \rho_0 R \tag{2.40}$$

In the classical formulation of the heat conduction problem, the heat capacity is considered constant and the heat flux is expressed by the Fourier law, often applied to an isotropic material. The strain rate driven by the immersion velocity V considered in the present study supports the hypothesis of a negligible value for the second term on the right hand side of (2.40). Summarizing, the linear momentum balance and the energy balance (in terms of entropy balance) are

$$\operatorname{Div} \mathbf{P} + \rho_0 \mathbf{B} = \rho_0 \ddot{\boldsymbol{\chi}} \tag{2.41}$$

$$\rho_0 C_v \dot{\vartheta} = k \triangle \vartheta + \rho_0 R \tag{2.42}$$

where the simbol $\triangle$ represents the laplacian of the absolute temperature ϑ.

The set constitutive equations reads:

$$\psi = \psi(\mathbf{C}, \vartheta) \tag{2.43}$$

$$\mathbf{P}(\mathbf{C}, \vartheta) = 2\mathbf{F}\frac{\psi(\mathbf{C}, \vartheta)}{\partial \mathbf{C}} \tag{2.44}$$

$$\eta(\mathbf{C}, \vartheta) = -\frac{\psi(\mathbf{C}, \vartheta)}{\partial \vartheta} \tag{2.45}$$

$$\mathbf{Q}(\mathrm{Grad}\,\vartheta) = -\mathbf{K}\,\mathrm{Grad}\,\vartheta, \tag{2.46}$$

where the thermal conductivity tensor $\mathbf{K}(\mathbf{X})$ is assumed to be positive definite and takes the form

$$\mathbf{K}(\mathbf{X}) = k(\mathbf{X})\mathbf{I} \tag{2.47}$$

for isotropic materials.

The simplification adopted for the present study lead to uncoupled governing equations: the problem can be solved computing separately the temperature field and using the temperature as a data for the solution of the mechanical response.

2.1.6 State functions for thermo-elastic materials

In the kinematics it is possible to adopt an operative point of view and decouple the volumetric inelastic thermal deformation gradient $\mathbf{F^a}$ and the elastic deformation $\mathbf{F^e}$, which represents the local stretch and distortion of the material lattice. When the external mechanical load is null, the elastic deformation is caused by the incompatibility of the thermal deformation field that prevents the full relaxation of the inelastic deformation due to the variation of the temperature in time. According to standard approach documented in the literature, we assume locally a multiplicative decomposition of the deformation gradient, as proposed by Kröner (1960) and Lee (1969)

$$\mathbf{F} = \mathbf{F^e}\mathbf{F^a} \tag{2.48}$$

Additionally we assume a form for the free energy, as presented by Yang and Ortiz [42], Stainier and Ortiz [38]

$$\psi(\mathbf{F^e}, \vartheta) = \psi^e(\mathbf{F^e}) + \rho_0 C_v \vartheta \left(1 - log\frac{\vartheta}{\vartheta_0}\right) \tag{2.49}$$

where ψ^e is the elastic strain energy density, ϑ_0 is a reference temperature. The strain energy density ψ^e depends solely on the elastic elastic part of the deformation tensor; material-frame indifference requires the dependence on the elastic right Cauchy-Green tensor

$$\mathbf{C^e} = \mathbf{F^{eT}F^e} = \mathbf{F^{a-T}CF^{a-1}} \tag{2.50}$$

2.1.7 Constitutive law: Isotropic Hyperelastic Model

The actual choice for the strain energy density is a neoHookean potential, extended to the compressible range:

$$\psi^e(\mathbf{F}^e) = \frac{1}{2}\lambda \log^2 J^e - \mu \log J^e + \frac{1}{2}\mu(I_1^e - 3)$$

The choice of a multiplicative decomposition leads to the particular formulation of the total stress in the form

$$\mathbf{P} = \frac{\partial \psi^e}{\partial \mathbf{F}} = \frac{\partial \psi^e}{\partial \mathbf{F}^e}\frac{\partial \mathbf{F}^e}{\partial \mathbf{F}} \tag{2.51}$$

where:

$$\frac{\partial \mathbf{F}^e}{\partial \mathbf{F}} = \mathbf{F}^{a-1}. \tag{2.52}$$

The elastic first Piola-Kirchhoff stress tensor reads:

$$\mathbf{P}^e = \frac{\partial \psi^e}{\partial \mathbf{F}^e} = \frac{\partial \psi}{\partial J^e}\frac{\partial J^e}{\partial \mathbf{F}^e} + \frac{\partial \psi}{\partial I_1^e}\frac{\partial I_1^e}{\partial \mathbf{F}^e} = (\lambda \log J^e - \mu)\,\mathbf{F}^{e-T} + \mu \mathbf{F}^e \tag{2.53}$$

The spatial elasticity tensor is:

$$\mathbb{C}^e = \frac{\partial^2 \psi}{\partial \mathbf{F}^e \partial \mathbf{F}^e} = \frac{\partial \mathbf{P}^e}{\partial \mathbf{F}^e} = \frac{\partial \mathbf{P}^e}{\partial J^e}\frac{\partial J^e}{\partial \mathbf{F}^e} + \frac{\partial \mathbf{P}^e}{\partial \mathbf{F}^{e-T}}\frac{\partial \mathbf{F}^{e-T}}{\partial \mathbf{F}^e} + \frac{\partial \mathbf{P}^e}{\partial \mathbf{F}^e} \tag{2.54}$$

$$= \lambda \mathbf{F}^{e-T} \otimes \mathbf{F}^{e-T} - (\lambda \log J^e - \mu)\, \mathbf{F}^{e-1} \odot \mathbf{F}^{e-1} + \mu \bar{\mathbb{I}} \tag{2.55}$$

The Piola-Kirchhoff stress tensor is:

$$\mathbf{P} = \frac{\partial \psi^e}{\partial \mathbf{F}^e}\frac{\partial \mathbf{F}^e}{\partial \mathbf{F}} = \left[(\lambda \log J^e - \mu)\mathbf{F}^{e-T} + \mu \mathbf{F}^e\right] \mathbf{F}^{a-1}. \tag{2.56}$$

The Cauchy stress $\boldsymbol{\sigma}$ is recovered as:

$$\boldsymbol{\sigma} = J^{-1}\mathbf{P}\mathbf{F}^T = J^{-1}\left[(\lambda \log J^e - \mu)\mathbf{F}^{e-T} + \mu \mathbf{F}^{eT}\right] \mathbf{F}^{a-1}\mathbf{F}^{aT}\mathbf{F}^{eT}. \tag{2.57}$$

Finally, the referential stiffness tensor is:

$$\mathbb{C} = \frac{\partial^2 \psi}{\partial \mathbf{F} \partial \mathbf{F}} = \frac{\partial \mathbf{P}}{\partial \mathbf{F}} = \frac{\partial \mathbf{P}}{\partial \mathbf{F}^e}\frac{\partial \mathbf{F}^e}{\partial \mathbf{F}} = \left(\frac{\partial \mathbf{F}^e}{\partial \mathbf{F}}\right)^T \frac{\partial \mathbf{P}^e}{\partial \mathbf{F}^e}\frac{\partial \mathbf{F}^e}{\partial \mathbf{F}} = \mathbf{F}^{a-T}\mathbb{C}^e\mathbf{F}^{a-1}. \tag{2.58}$$

The second Piola-Kirchhoff stress tensor is recovered as

$$\mathbf{S} = \mathbf{F}^{-1}\mathbf{P} = \mathbf{F}^{a-1}\mathbf{F}^{e-1}\left[(\lambda \log J^e - \mu)\mathbf{F}^{e-T} + \mu \mathbf{F}^e\right] \mathbf{F}^{a-1} \tag{2.59}$$

$$= \mathbf{F}^{a-1}\left[(\lambda \log J^e - \mu)\mathbf{F}^{e-1}\mathbf{F}^{e-T} + \mu \mathbf{I}\right] \mathbf{F}^{a-1} \tag{2.60}$$

$$= \mathbf{F}^{a-1}\left[(\lambda \log J^e - \mu)\mathbf{C}^{e-1} + \mu \mathbf{I}\right] \mathbf{F}^{a-1}. \tag{2.61}$$

A simple choice for the thermal deformation gradient is to assume a fully volumetric expansion, therefore we write:

$$\mathbf{F}^a = (1 + \alpha\delta\vartheta)\,\mathbf{I} \tag{2.62}$$

$$\mathbf{F}^{a-1} = \frac{1}{(1 + \alpha\delta\vartheta)}\mathbf{I} \tag{2.63}$$

the second Piola-Kirchhoff stress tensor may be computed as follow

$$\mathbf{S} = \frac{1}{(1+\alpha\delta\vartheta)^2}\left[(\lambda \log J^e - \mu)\mathbf{C}^{e-1} + \mu\mathbf{I}\right] \tag{2.64}$$

Recalling the definition of the stress-temperature modulus

$$\mathbf{M}(\mathbf{C},\vartheta) = \frac{\partial \mathbf{S}(\mathbf{C},\vartheta)}{\partial\vartheta} = \frac{-2\alpha}{(1+\alpha\delta\vartheta)}\left[(\lambda \log J^e - \mu)\mathbf{C}^{e-1} + \mu\mathbf{I}\right] \tag{2.65}$$

we obtain an expression that may be use in the heat equation (2.42) in cases where the strain rate becomes relevant for the problem, i.e. if the immersion velocity V takes values with order of magnitudes $3-4$ times larger than the one we are focused on.

2.2 Fracture

2.2.1 Irreversible Cohesive Fracture model in a Non-linear kinematics framework.

A simple cohesive law allows to describe fracture nucleation ad propagation through only two material parameters: the peak cohesive traction and the fracture energy of the material. The cohesive theory of fracture since its first theorical formulation due to Dugdale [10] Barenblatt [1], Rice and others regards the fracture as a gradual phenomenon in which separation takes place across an "extended" crack tip (cohesive zone) and it is resisted by cohesive tractions t. This approach can be endowed into the material independently of its peculiarity like the constitutive behaviour of the bulk or the characteristic size of the *process zone*. The process zone defines a region around the crack tip in which inelastic deformation takes place and where the fracture energy is dissipated through a progressive de-bonding that leads to the formation of new surfaces. Traditionally, in finite element analysis, cohesive approaches have been embedded in specific *cohesive finite elements* [4] [28]. Surface-like elements are compatible with the general bulk discretizations of the solid.

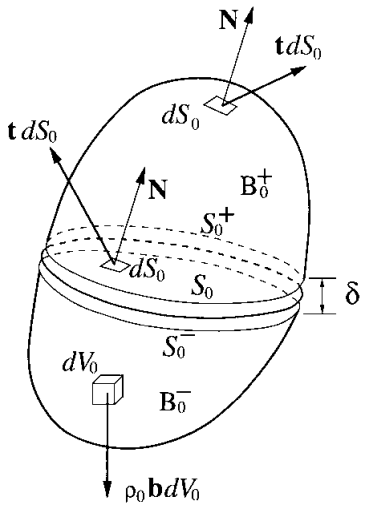

Figure 2-1: Cohesive surface traversing a 3D body

We assume that the volume Ω of the body B is traversed by a cohesive surface S_{coh} which partitions the body into two subbodies $\Omega^{\pm}$, lying on the the two sides of S_{coh}. The deformation power, i.e., the power committed by the system in the elastic and inelastic deformations, is then represented by the part of the mechanical power expended on the solid by external (volume and surface) forces non applied in rising its kinetic energy:

$$\dot{\psi} = \dot{\psi}^{ext} - \dot{K} = \sum_{\pm} \int_{\Omega^{\pm}} \rho(\mathbf{B} - \ddot{\boldsymbol{\chi}}) \cdot \dot{\boldsymbol{\chi}} \, dV + \sum_{\pm} \int_{\partial\Omega^{\pm}} \mathbf{T} \cdot \dot{\boldsymbol{\chi}} \, dS \tag{2.66}$$

The kinetic energy is given by the sum of the quantities computed over the two sub-bodies

$$K = \sum_{\pm} \int_{\Omega^{\pm}} \frac{1}{2} \rho \mid \dot{\boldsymbol{\chi}} \mid^2 \, dV \tag{2.67}$$

The balance of tractions on the external surface of the sub-bodies and on the cohesive interface:

$$\mathbf{PN} = \mathbf{T} \qquad \text{on} \qquad \partial\Omega^{\pm} \tag{2.68}$$

$$[\![\mathbf{PN}]\!] = [\![\mathbf{t}]\!] = 0 \qquad \text{on} \qquad \partial S^{\pm}_{coh} \tag{2.69}$$

leads to the strain energy for a cohesive solid of the form

$$\int_{\Omega} \mathbf{P} : \mathbf{F}\, dV + \int_{S_{coh}} \mathbf{t} \cdot [\![\boldsymbol{\chi}]\!]\, dS. \tag{2.70}$$

From (2.70) the duality or work-conjugacy relations between stress and strain measures can be discerned by distinguish:

- over the bulk of the body, as in conventional solids, the first Piola-Kirchhoff stress tensor $\mathbf{P}$ is work-conjugate to the deformation gradients $\mathbf{F}$;
- over the cohesive surface, the tractions $\mathbf{t}$ are work-conjugate to the displacement jumps or *opening displacement* $\delta = [\![\boldsymbol{\chi}]\!]$.

The second integral in eq. (2.70) is defined over S_{coh}, which, given the presence of two flanks, needs to be defined explicitly. We refer to the cohesive surface as the "average" of the two interface surfaces ${S_{coh}}^{+}$ and ${S_{coh}}^{-}$

$$\overline{\boldsymbol{\chi}} = \frac{1}{2}(\boldsymbol{\chi}^{+} + \boldsymbol{\chi}^{-}) \tag{2.71}$$

and the mapping of the two flanks becomes:

$$\boldsymbol{\chi}^{\pm} = \overline{\boldsymbol{\chi}} \pm \frac{1}{2}\boldsymbol{\delta} \tag{2.72}$$

Pandolfi and Ortiz [28] postulate the existence of a free energy density per unit of undeformed area over S_{coh} in the general form

$$\phi = \phi(\boldsymbol{\delta}, \vartheta, \mathbf{q}; \operatorname{Grad} \overline{\boldsymbol{\chi}}) \tag{2.73}$$

as a function of the local temperature ϑ and of a collection of suitable internal variables $\mathbf{q}$ able to describe the inelastic process of decohesion. The surface deformation described by $\operatorname{Grad} \overline{\boldsymbol{\chi}}$ is included into the formulation to take into account possible anisotropic behaviour of the material, since for isotropic materials a change of $\overline{\boldsymbol{\chi}}$ at constant δ does not imply any decohesion or crack closure. By assuming that the

cohesive behavior derives from a free energy density ϕ, the cohesive law reads:

$$\mathbf{t} = \frac{\partial \phi}{\partial \boldsymbol{\delta}} \tag{2.74}$$

Irreversibility requires the definition of an evolution law for the internal variables $\mathbf{q}$, governed by a kinetic relation of general form

$$\dot{\mathbf{q}} = \dot{\mathbf{q}}(\boldsymbol{\delta}, \vartheta, \mathbf{q}). \tag{2.75}$$

For simplicity we disregard the dependencies on the temperature and on the deformation of stretching and shearing of the cohesive surface. It follows that the free energy density must be of the simpler form

$$\phi = \phi(\delta_n, \boldsymbol{\delta} \cdot \operatorname{Grad} \overline{\boldsymbol{\chi}}, \mathbf{q}). \tag{2.76}$$

Material isotropy allows to assume the response to sliding as independent of the direction and to consider only the dependence on the the norm $\mid \boldsymbol{\delta}_S \mid = \delta_S$ of the sliding component of the crack opening displacement. The energy density and surface traction can be written as

$$\phi = \phi(\delta_n, \delta_S, \mathbf{q}) \tag{2.77}$$

$$\mathbf{t} = \frac{\partial \phi}{\partial \delta_n}(\delta_n, \delta_S, \mathbf{q})\mathbf{n} + \frac{\partial \phi}{\partial \delta_S}(\delta_n, \delta_S, \mathbf{q})\frac{\boldsymbol{\delta}_S}{\delta_S}. \tag{2.78}$$

In [4] a further semplification was introduced by reducing the opening displacements to a scalar valued effecttive one

$$\delta = \sqrt{\beta_2 \delta_S^2 + \delta_n^2} \tag{2.79}$$

which is adopted also in the expression of the fre energy

$$\phi = \phi(\delta, \mathbf{q}). \tag{2.80}$$

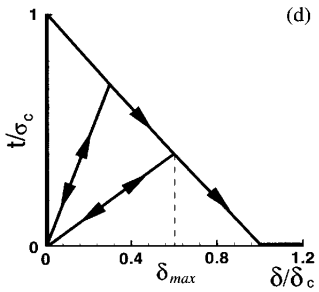

Figure 2-2: Adopted cohesive law expressed in terms of an effective opening displacement δ and a traction t: loading-unloading rule from linearly decreasing loading envelop.

Under this condition the cohesive law assumes the expression

$$\mathbf{t} = \frac{t}{\delta}(\beta^2 \boldsymbol{\delta}_S + \delta_n \mathbf{n}) \tag{2.81}$$

where t is the scalar effective traction derived from ϕ through the effective opening displacement

$$t = \frac{\partial \phi}{\partial \delta}(\delta, \mathbf{q}) = \sqrt{\beta^{-2} \mid \mathbf{t}_S \mid^2 + {t_n}^2} \tag{2.82}$$

The factor β defines the ratio between the shear and the normal critical tractions. Upon closure the cohesive surfaces are subjected to the contact unilateral constraint including friction. These surfaces interactions may be modeled as independent phenomena, but the aim of the present work is simply to characterize the cohesive law with an irreversibility property by defining a suitable unloading law. An appropriate choice of the internal variable set $\mathbf{q}$ reduces to the maximum ever attained effective opening displacement δ_{max}. Loading is characterized by the conditions

$$\delta = \delta_{max}\,; \qquad \dot{\delta} \geq 0 \tag{2.83}$$

We adopt a cohesive law represented by a piecewise linear function, as depicted in Fif.2-2. The sketch illustrates the rule of unloading to the origin, as introduced in

[4], i.e.,

$$t = \frac{T_{max}}{\delta_{max}}\delta \qquad \text{if} \qquad \delta < \delta_{max}\,; \qquad \dot{\delta} < 0 \tag{2.84}$$

Chapter 3

Numerical procedure

3.1 Heat conduction problem

Let us recall the equations of the energy balance (2.41), (2.42)

$$\mathrm{Div}\,\mathbf{P} + \rho_0 \mathbf{B} = \rho_0 \ddot{\boldsymbol{\chi}} \tag{3.1}$$

$$\rho_0 C_v \dot{\vartheta} = k \triangle \vartheta + \rho_0 R \tag{3.2}$$

The energy balance equation represents the heat conduction law of a solid and it may be recast as follow

$$\dot{\vartheta} = \kappa \triangle \vartheta + \frac{R}{C_v} \tag{3.3}$$

Eq. (3.3) represents the diffusion parabolic equation of the transient heat problem. Assuming no source of radiant heat into the body and we consider negligible the time derivative of the temperature ϑ, adopting the elliptic Laplace equation of the steady heat problem. This choice is supported by the analysis of the Biot number relative to the particular set of experimental results which is the scope of the present research. For more detail we refer to the section 1.3.3. The formulation of the boundary value

thermal problem [35], [30] may be written

$$-\kappa \triangle \vartheta = 0 \qquad \text{in } \Omega \tag{3.4}$$

$$\vartheta = \vartheta_0 \qquad \text{on } \Gamma_{cold} \tag{3.5}$$

$$\vartheta = \vartheta_0 + \Delta\vartheta \qquad \text{on } \Gamma_{hot} \tag{3.6}$$

The Dirichlet non-homogeneus boundary conditions (3.5) and (3.6) are represented by the temperature we impose to the node belonging the cold subdomanin Γ_{cold} (supposed to be at water temperature) or to the hot one Γ_{hot} (supposed to be kept at the oven temperature). The solution of the problem is well known and it is represented by a linear distribution of the temperature in the spatial gap between the cold and hot reservoir where the temperature is imposed to be constant. This assumption has been justified by analysing the conditions for thermal process in the section 1.3.3.

3.2 Weak form and discretization of the mechanical problem

3.2.1 Weak Form

We restate the linear momentum balance (2.41) in index notation, imposing the boundary conditions and removing the body force term, not relevant for this problem.

$$\begin{aligned} \operatorname{Div} \mathbf{P} &= \rho_0 \ddot{\boldsymbol{\chi}} \quad \text{in } B \times (0,T) \\ \boldsymbol{\chi} &= \bar{\boldsymbol{\chi}} \quad \text{on } \Gamma_D \times (0,T) \\ \mathbf{PN} &= \bar{\mathbf{T}} \quad \text{on } \Gamma_N \ \times (0,T) \text{ Neumann boundary} \end{aligned}$$

where Γ_D and Γ_N are on disjoint part of the boundary of B representing respectively the Dirichlet and Neumann boundary. The non-linear mechanical problem is defined on the domain $B \subset \mathbb{R}^2$ and over the time interval $(0,T) \in \mathbb{R}_+$, with mixed

boundary conditions represented by displacements and tractions imposed Γ_D and Γ_N and completed by the initial conditions

$$\boldsymbol{\chi}|_{t=0} = \boldsymbol{\chi}_0$$
$$\dot{\boldsymbol{\chi}}|_{t=0} = \dot{\boldsymbol{\chi}}_0$$

To obtain the equivalent variational form of problem that is amenable to discretization, we introduce the power functional $J : X \mapsto \mathbb{R}$

$$J(\dot{\boldsymbol{\chi}}) = \underbrace{\int_{\Gamma_N} \bar{\mathbf{T}} \cdot \dot{\boldsymbol{\chi}}\, dS}_{W^{\text{ext}}} - \underbrace{\frac{d}{dt}\int_B \frac{1}{2}\rho_0 \|\dot{\boldsymbol{\chi}}\|^2\, dV}_{\dot{K}} - \underbrace{\int_B \dot{\psi}\, dV}_{W^{\text{int}}} \tag{3.7}$$

with energetic aspects of the problem condensed in the following terms:

- W^{ext} is external power expended on body.
- $\dot{K}$ is rate of change of kinetic energy of body
- W^{int} is the power arising from the deformation of the body. It includes no form of dissipation, to be consistent with the reversible modeling here in force.

In the next equations the arguments $(\mathbf{X}, t)$ of all fields are suppressed for the sake of clarity.

Admissible trial deformation mappings belong to a non-linear space

$$X = \left\{ \boldsymbol{\chi} \in [H^1(B)]^2 \times C^1((0,T)) \middle|\, \boldsymbol{\chi}|_{\Gamma_D} = \bar{\boldsymbol{\chi}} \right\} \tag{3.8}$$

due to the presence of inhomogeneous boundary conditions. Function space of admissible spatial variations is

$$V = \left\{ \mathbf{v} \in [H^1(B)]^2 \times C^0((0,T)) \middle|\, \mathbf{v}|_{\Gamma_D} = \mathbf{0} \right\} \tag{3.9}$$

The equivalent variational form of the momentum balance states that the first variation of the power functional vanishes when tested against all admissible variations

i.e.

$$\langle DJ(\dot{\boldsymbol{\chi}}); \dot{\boldsymbol{\eta}} \rangle = 0 \quad \forall \dot{\boldsymbol{\eta}} \in V \tag{3.10}$$

Taking the directional derivative of the energy functional we obtain

$$\langle DJ(\dot{\boldsymbol{\chi}}); \dot{\boldsymbol{\eta}} \rangle = \frac{d}{d\varepsilon} J(\dot{\boldsymbol{\chi}} + \varepsilon \dot{\boldsymbol{\eta}})|_{\epsilon=0} \tag{3.11}$$

$$= \int_{\Gamma_N} \bar{\mathbf{T}} \cdot \dot{\boldsymbol{\eta}} \, dS - \int_B \rho \ddot{\boldsymbol{\chi}} \cdot \dot{\boldsymbol{\eta}} \, dV - \int_B \mathbf{P} : \operatorname{Grad} \dot{\boldsymbol{\eta}} \, dV \tag{3.12}$$

Hence the weak form of the mechanical problem is find $\boldsymbol{\chi} \in X$ such that

$$\int_{\Gamma_N} \bar{\mathbf{T}} \cdot \dot{\boldsymbol{\eta}} \, dS - \int_B \mathbf{P} : \operatorname{Grad} \dot{\boldsymbol{\eta}} \, dV = \int_B \rho_0 \ddot{\boldsymbol{\chi}} \cdot \dot{\boldsymbol{\eta}} \, dV \tag{3.13}$$

for all $\dot{\boldsymbol{\eta}} \in V$.

3.2.2 Spatial Discretization

To be able to adopt numerical tecnique and computational implementation for solving the mechanical problem, we perform a semi-discretization in space of the weak form 3.13 with the finite element method.

We form a shape-regular, pairwise disjoint triangulation $\mathcal{T}$ of B, comprising triangles K. We choose standard discrete function spaces $X_h \subset X$ and $V_h \subset V$ to interpolate field variables

$$X_h = \{ \boldsymbol{\chi}_h \in X | \, \boldsymbol{\chi}_h|_K = \mathcal{P}_n \; \forall K \in \mathcal{T}_h \} \tag{3.14}$$

$$V_h = \{ \mathbf{v} \in V | \, \mathbf{v}_h|_K = \mathcal{P}_n \; \forall K \in \mathcal{T}_h \} \tag{3.15}$$

As in the standard Galerkin finite elements formulation, the function spaces V_h and X_h coincide (apart from Dirichlet boundary). In all the simulation we adopt quadratic polynomial interpolating functions, so we have $n = 2$.

The finite element approximation of the body motion is described as a linear

combination of the nodal values of the function

$$\boldsymbol{\chi}_h = \sum_b N^b(\mathbf{X})\mathbf{x}^b(t) \qquad\qquad \dot{\boldsymbol{\eta}} = \sum_a N^a(\mathbf{X})\boldsymbol{\eta}^a(t) \tag{3.16}$$

$$\tag{3.17}$$

where $\mathbf{X}^b$ and $\boldsymbol{\eta}^a$ are the nodal coefficients of the basis functions N^a, N^b ,with indices a, b each ranging over all the nodes in the mesh.

The time derivatives follow

$$\dot{\boldsymbol{\chi}}_h = \sum_b N^b \dot{\mathbf{x}}^b \qquad\qquad \ddot{\boldsymbol{\chi}}_h = \sum_b N^b \ddot{\mathbf{x}}^b \tag{3.18}$$

likewise $\operatorname{Grad}\dot{\boldsymbol{\eta}} = \sum_a \operatorname{Grad} N^a \otimes \boldsymbol{\eta}^a$.

Substituting the definitions into 3.13, we obtain a discreat version of the weak form

$$\sum_a \eta_i^a \left[\int_{\Gamma_N} \bar{T}_i N^a \, dS - \int_B (P_h)_{iJ} \, N^a_{,J} \, dV - \left(\sum_b \int_B \rho_0 N^a N^b \, dV \ddot{x}_i^b \right) \right] = 0_i \tag{3.19}$$

which must hold for all $\dot{\boldsymbol{\eta}} \in V_h$. The discrete Piola-Kirchoff stress is computed directly from the discrete deformation mapping using

$$\mathbf{P}_h = \mathbf{P}(\mathbf{F}_h), \quad \mathbf{F}_h = \operatorname{Grad}\boldsymbol{\chi}_h = \sum_b \operatorname{Grad} N^b \otimes \mathbf{x}^b$$

Eq. 3.19 places no constraint on the η_i^a , and hence the above holds if and only if each term of the sum vanishes independently. We express this condition in a compact matrix form

$$\mathbf{F}^a_{\text{ext}} - \mathbf{F}^a_{\text{int}} = \mathbf{M}^{ab}\ddot{\mathbf{x}}^b \tag{3.20}$$

with the following definitions

- external forces: $F_i^a{}_{\text{ext}} = \int_{\Gamma_N} \bar{T}_i N^a \, dS$

- internal forces: $F^a_{i\,\mathrm{int}} = \int_B (P_h)_{iJ}\, N^a_{,J}\, dV$
- mass matrix: $M^{ab} = \int_B \rho_0 N^a N^b\, dV$

and implying the summation over nodal index b. These calculations are carried out on an element-by-element basis. According to the standard F.E. approach, the local contribution is computed by restricting the support of the basis functions to the single element and summed to the global arrays above at shared nodes.

The semi-discrete equations (3.20) describe a transient dynamic process, so it needs to be discretized also in time. For the static problem we are dealing with null acceleration. The necessity of including the term relative to the acceleration is justified by the numerical strategy applied for solving the static problem. The dynamic relaxation technique, indeed, regards the statical solution as the steady-state response of the system, combined with the explicit Newmark algorithm to carry the time integration.

Operatively, the mass matrix is *not* calculated using an approximation that renders the matrix diagonal. This simplification leads to large savings in computational effort, reducing the solving system into a set of independent equations. In general the substitution of the consistent mass matrix with the diagonal lumped one does not affect the accuracy of the solution in a relevant way, while it helps in reducing the computational time [19] It is particularly favorable in our case, since the specific transient solutions represent an artificial expedient.

3.3 Dynamic Relaxation

The problem we are analyzing represents an example of a system in quasi-static conditions undergoing instability phenomena. This means that the algorithm solving the mechanical problem, has to be able to detect possible bifurcation points and to follow the evolution of the unstable behaviour.

A suitable tool for this purpouse is the *dynamic relaxation* tecnique, which consistes of determining the steady-state response to the transient dynamic analysis for

an autonomous system. In this case the transient part of the solution is of no interest, the desired outcome is represented by the steady-state response of the system.

Regarding the whole problem a reduced loading time step is usually required to ensure the capturing of particular configurations. The computational cost per time step is minimal and is mostly associated with the evaluation of the internal force vector $\mathbf{F}_{int}$. The assembly and storage of a global stiffness matrix is not required and this allows the treatment of complex material models. Being a critically damped process, the dynamic relaxation algorithm is generally slow but reliable and it has the potential for efficient implementation on a wide range of high-performance parallel computer architectures.

The discretized equations of motion governing the dynamic response, for the nth artificial time increment, may be written as follow:

$$\mathbf{M}\ddot{\mathbf{x}}^n + c\mathbf{M}\dot{\mathbf{x}}^n + \mathbf{F}_{int}(\mathbf{x}^n) = \mathbf{F}_{ext}^n \tag{3.21}$$

where $\mathbf{M}$ is a mass matrix, c is the damping coefficient for mass-proportional damping, $\mathbf{F}_{int}$ is the internal force vector, and $\mathbf{F}_{ext}^n$ is a vector of external loads at the current time step. The vectors $\ddot{\mathbf{x}}^n$, $\dot{\mathbf{x}}^n$ and $\mathbf{x}^n$ represent the acceleration, velocity and displacement vectors, respectively. A diagonal mass matrix obtained by mass lumping, as well as a diagonal mass-proportional damping matrix, leads to a decoupled set of algebraic equations, where each solution component may be computed independently.

In the present approach the solution of (3.3) is obtained by applying an explicit time integration method with central-difference scheme (Newmark iterative procedure).

$$\dot{\mathbf{x}}^{n+1/2} = \frac{1}{\Delta t}\left(\mathbf{x}^{n+1} - \boldsymbol{\chi}^n\right) \tag{3.22}$$

$$\ddot{\mathbf{x}}^n = \frac{1}{\Delta t}\left(\dot{\mathbf{x}}^{n+1/2} - \dot{\mathbf{x}}^{n-1/2}\right) \tag{3.23}$$

where Δt is the artificial time step. The implementation of dynamic relaxation en-

sures large stability limits and optional parallel implementation. The objective of the adaptive dynamic relaxation algorithm for a static analysis is to reach the steady-state solution of a critically damped pseudo-transient response. The mass and damping parameters do not represent the physical system, hence they are artificially defined in order to produce the fastest convergence to the steady-state solution. The convergence criterion is based on a relative error of the residual force:

$$\epsilon = \frac{\|\mathbf{F}_{ext} - \mathbf{F}_{int}\|}{\|\mathbf{F}_{ext} + \mathbf{F}_{int}\|} \leq \epsilon_{tol} \tag{3.24}$$

3.3.1 Integration parameters

The dynamic relaxation integration parameters for static analysis consist of the diagonal mass matrix $\mathbf{M}$, damping coefficient c and time step Δt. They can be determined on the basis of simple observations. The stability condition for explicit analysis imposes an upper limit for the time step driven by the minimum size of the finite elements of the discretized body. The stable time step is estimated as the quotient between the mesh size and the elastic longitudinal wave speed for the material:

$$\Delta t \leq min_e \left(\frac{h}{s}\right)_e \tag{3.25}$$

A value of c which critically damps the system and implies a fast convergence to the steady state is estimated by the following ratio, as documented by Oakley and Knight in [27]:

$$c \simeq \frac{2\omega_0\omega_m}{\sqrt{\omega_0^2\omega_m^2}} \tag{3.26}$$

being ω_0 and ω_m the minimum and maximum frequency of the discretized system. The value of the minimum natural frequency of a mechanical system is usually much smaller of the maximum one. This lead to the following approximated expression:

$$c \simeq 2\omega_0 \tag{3.27}$$

An estimate of the minimum eigenvalue ω_0^2 is represented by the stiffness-mass Rayleigh quotient

$$\omega_0^2 \simeq \frac{\mathbf{v^T K v}}{\mathbf{v^T M v}} \tag{3.28}$$

where $\mathbf{v}$ is a generic weighting vector and $\mathbf{K}$ is is the stiffness matrix (for linear problems). The following diagonal approximation of the tangent stiffness matrix can be assumed for non linear problems:

$$K_{ii} = \frac{\mathbf{F}_{int\,i}(\mathbf{x}^{n+1}) - \mathbf{F}_{int\,i}(\mathbf{x}^{n})}{\mathbf{x}^{n+1} - \mathbf{x}^{n}}. \tag{3.29}$$

In particular, assuming as weighting vector the difference

$$\mathbf{v} = \mathbf{x}^{n+1} - \mathbf{x}^{n} \tag{3.30}$$

the Rayleigh quotient becomes

$$\omega_0^2 = max\left(\frac{(\mathbf{x}^{n+1} - \mathbf{x}^{n})^{\mathbf{T}}(\mathbf{F}_{int}^{n+1} - \mathbf{F}_{int}^{n})}{(\mathbf{x}^{n+1} - \mathbf{x}^{n})^{\mathbf{T}} \cdot \mathbf{M}(\mathbf{x}^{n+1} - \mathbf{x}^{n})}\,,\,0\right) \tag{3.31}$$

For problems which exhibit structural instabilities the stiffness matrix may loose positive definiteness. When this occurs, the lowest eigenvalue may become negative and the damping coefficient c is set equal to zero.

In non-linear problems the integration parameters must be updated in an adaptive manner in order to maintain stable and efficient convergence. The version of Dynamic Relaxation with parameter updates is called [41] Adaptive Dynamic Relaxation.

3.4 Fracture

The propagation of the fracture is explicitly implemented in the finite element model, so that cracks can branch, coalesce and eventually produce fragments. The creation of a new fracture surface is accomplished by allowing initially coherent inter-elements

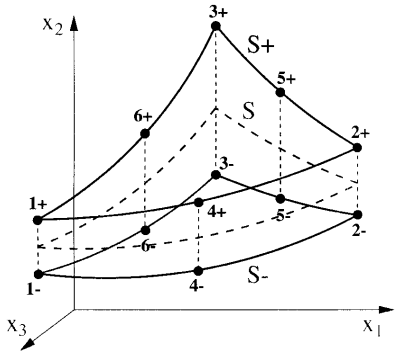

(a) Geometry of cohesive element composed by the surfaces S^- S^+

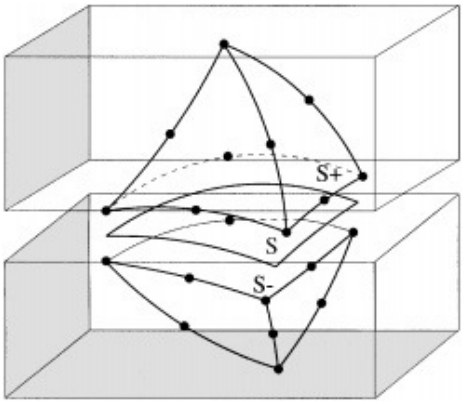

(b) Triangular cohesive element with 12 node

Figure 3-1: Geometry of tringular cohesive element inserted between two 10-node tetrahedral elements

boundaries to open according to a cohesive law which models a gradual loss of strength with increasing flanks separation. The choice of the cohesive law defines the work of separation, or fracture energy, required for creating a new free surface.

3.4.1 Finite element implementation of fracture

Rather than implementing the cohesive law as a mixed boundary condition we directly embed the cohesive law into surface-like finite elements. The cohesive elements consists of two surface elements S^- S^+ (figure 3-1a) which concide in space in the reference configuration of the solid. Each of the elements has n nodes and the total number of nodes is therefore $2n$. The figure 3-1b represents in particolar the geometry of triangular cohesive elements compatible with three-dimensional tetraedral elements. We denote by $N^a(s_1, s_2)$, $a = 1, \ldots, n$ the standard shape functions of the cohesive elements, being (s_1, s_2) the natural coordinates of each surface elements in some convenient standard configuration. The calculation require a continuous tracking of the tangential and normal direction. Since S^- S^+ may diverge by a finite distance, we uniquely define the normal $\mathbf{n}$ on the middle surface S, parametrically

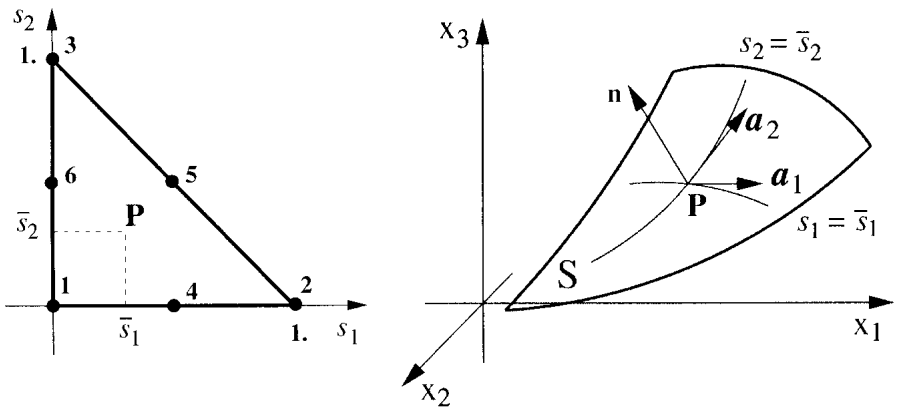

Figure 3-2: (a) Standard element configuration and natural co-ordinate system; (b) deformed middle surface S and corresponding curvilinear coordinate system.

defined as

$$\mathbf{x}(\mathbf{s}) = \sum_{a=1}^{n} \overline{\mathbf{x}}^a N^a(\mathbf{s}) \tag{3.32}$$

where

$$\overline{\mathbf{x}}^a = \frac{1}{2}\left(\mathbf{x}^{a+} + \mathbf{x}^{a-}\right) \tag{3.33}$$

and $\mathbf{x}^{a\pm}$, $a = 1, \ldots, n$ are the coordinates of the nodes of the cohesive elements in their deformed configuration. The tangent basis vectors of the curvilinear coordinate system defined by (s_1, s_2) for the middle surface correspond to

$$\mathbf{a}_{,\alpha}(\mathbf{s}) = \sum_{a=1}^{n} \overline{\mathbf{x}}^a N^a_{,\alpha}(\mathbf{s}) \qquad\qquad \alpha = 1, 2 \tag{3.34}$$

The unit normal which points from S^- to S^+ becomes

$$\mathbf{n} = \frac{\mathbf{a}_1 \times \mathbf{a}_2}{\mid \mathbf{a}_1 \times \mathbf{a}_2 \mid} \tag{3.35}$$

In the spatial configuration we compute also the opening displacement vector (see

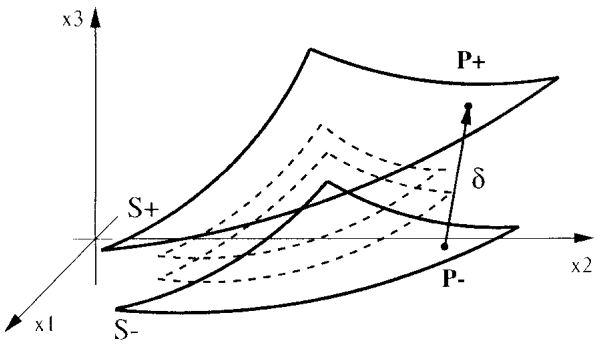

Figure 3-3: Opening displacement

figure 3-3)

$$\boldsymbol{\delta}(\mathbf{s}) = \sum_{a=1}^{n} [\![\mathbf{x}^a]\!] \, N^a(\mathbf{s}) \tag{3.36}$$

where

$$[\![\mathbf{x}^a]\!] = \mathbf{x}^{a+} - \mathbf{x}^{a-} \tag{3.37}$$

shows as $\boldsymbol{\delta}$ is invariant upon sumperimposed rigid body motions. The cohesive traction vector compatible with the adopted model may be defined per unit of undeformed area as follow

$$\mathbf{t} = \mathbf{t}(\boldsymbol{\delta}, \mathbf{n}) = \frac{t}{\delta} \left[\beta^2 \boldsymbol{\delta} + \left(1 - \beta^2\right) (\boldsymbol{\delta} \cdot \mathbf{n}) \, \mathbf{n} \right] \tag{3.38}$$

The dependence of $\mathbf{t}$ on the normal needs to be take into account into the finite element implementation. The nodal forces arised from the tractions are computed as integral extend over the undeformed surface of the element in its reference configuration as follow

$$F_i^{a\pm} = \mp \int_{S_{coh}} t_i N^a dS \tag{3.39}$$

There is no need to compute the stiffness matrix relative to fracture contribution, the algorithm adopted for the mechanical problem does not require the solution of a

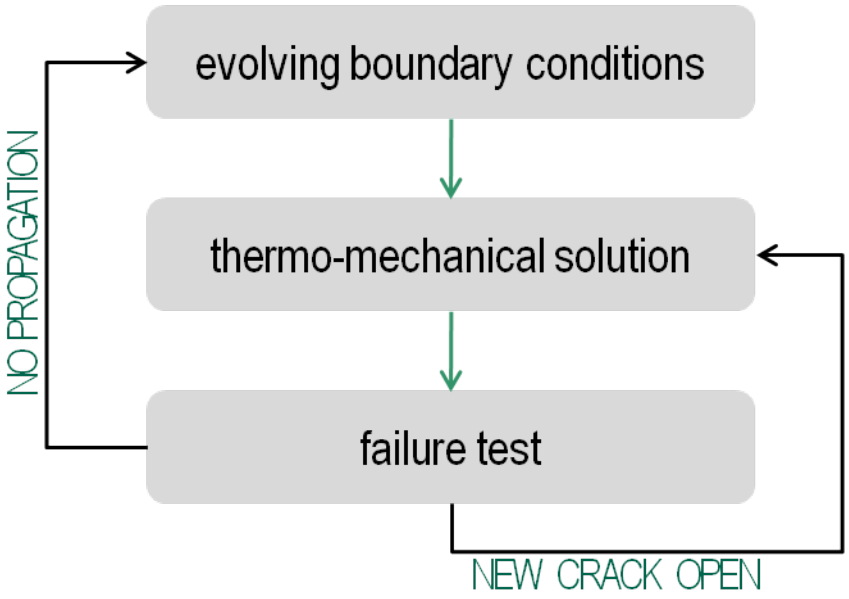

Figure 3-4: Flow chart of the numerical procedure for the solution of the thermo-mechanical problem and the detection of fracture propagation.

linear system of equations.

3.5 Synthesis of the numerical strategy

The numerical procedure implemented in the finite element code consists of a few logical operations repeated at each time step. As first, evolving boundary conditions, represented by nodal temperature, are applied according to the steady thermal profile already described and motivated. The consequent inelastic volumetric expansions are computed and imposed as input for the mechanical problem. Through the dynamic relaxation technique the solution to the mechanical problem is obtained and in particular the stress field within the plate becomes know. The failure test is performed at each element boundary interface by comparing the traction forces applied with a critical value. If the test is positive a new cohesive element is inserted, the continuity condition between the elements is removed and the topology is updated. Within the same fracture iteration, a mechanical analysis follows the opening of a new facet in order to re-compute the value of the deformation and stress tensors. At each time step the failure test is repeated as long as its outcome is positive and the fracture can

be extended. If the test fails, no crack propagation needs to be accounted and the procedure can move on to the next time step.

Chapter 4

Numerical results

4.1 Numerical test setup.

In order to simulate the instability of the direction of crack propagation, we have developed a numerical code. Assumptions on the governing equations of our model have been discussed in the previous sections. We proceed explaining some of the details of the implementation and presenting the results so far produced.

The mechanical problems is discretized by a two-dimensional finite element model with quadratic triangular elements. The heat conduction process is simulated by imposing evolving temperature conditions, represented by an assigned thermal profile:

i) the water temperature ϑ_0 imposed on the node gradually immersed into the bath;

ii) a linear increasing temperature (from ϑ_0 to $\vartheta_0 + \Delta\vartheta$ over the length H) in the area between the cold and hot reservoir;

iii) the initial plate temperature $\vartheta_0 + \Delta\vartheta$ associated to the node of the top part of the sample.

This Dirichlet type boundary conditions change in time according to the descent velocity characterizing the experiment.

The thermal strains, computed on the basis of the local temperature, are assumed as datum of the mechanical problem. The stress state induced by inhomogeneous

thermal expansion develops in correspondence of the non-negligible second spatial derivative of the temperature field and it is perturbed by the presence of the growing crack.

An isotropic, non linear, hyperelastic model is adopted for the bulk material. Dissipative behaviours only manifest in the process zone ahead of the crack tip and it is accounted by the cohesive law. The cohesive model is based on the definition of an effective fracture opening displacement δ, work conjugate to an effective fracture traction t. The two scalar quantities are defined based on the corresponding vectors, assigning different weights to the normal and to the tangential components. The crack is allowed to propagate, from the initial notch tip, only between the interfaces of the original elements, when the effective traction reaches a critical value defined by the chose fracture criterion

$$t = \sqrt{\beta^{-2} \mid \mathbf{t}_S \mid^2 + {t_n}^2} \leq t_{cr}. \tag{4.1}$$

Fracture is then simulated via the local introduction of 3-node cohesive elements in between the original elements, through an auto-adaptive re-meshing procedure. The cohesive law governs the subsequent effective opening process along the new surfaces.

4.2 Qualitative discussion on the crack patterns resulting from the simulations.

The main set of numerical experiments has been performed by keeping constant material and geometry of the sample and varying the temperature gap $\Delta\vartheta$ and the immersion speed V, in order to investigate the dependance of the results on these two parameters.

The Fig.4-1 summarizes the global fracture behaviour according to three classes of patterns:

i) straight crack (symbol in Fig.4-1: +);

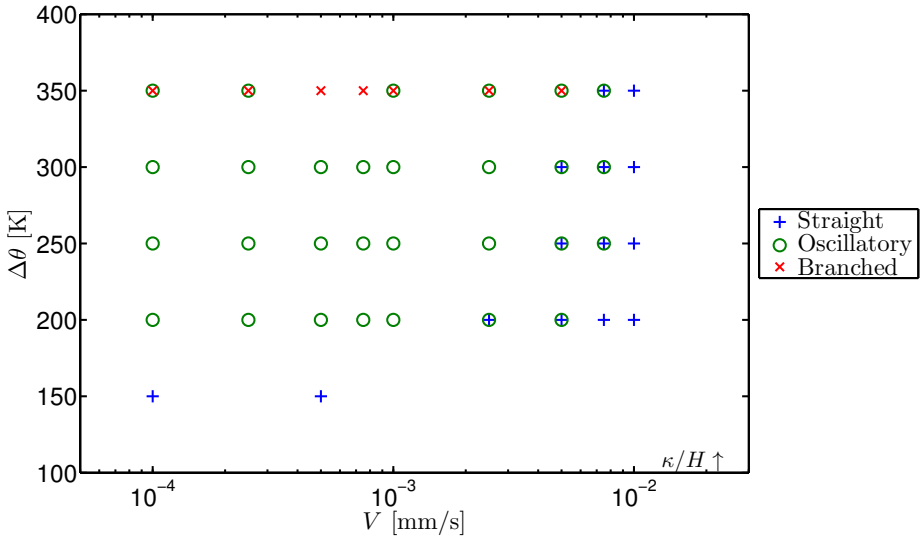

Figure 4-1: Phase Field of the crack morphology, depending on the parameters: V and $\Delta\vartheta$. The value κ/H represents the limit of validity of the steady thermal state assumption.

ii) oscillating crack (symbol in Fig.4-1: o);

iii) branched crack (symbol in Fig.4-1: x);

the combination of two symbols accounts for mixed patterns.

The cold reservoir is at the constant temperature 20 °C, the temperature of the hot region varies, according to $\Delta\vartheta$, assuming alternatively the values: 220, 270, 320, 370. Nine different immersion velocity over the range 0.0001mms^{-1} - 0.01mms^{-1} have been tested.

We collect here the crack patterns relative to each simulated case, in order to extract some considerations:

i) The finite element discretization of the problem, the non-linear kinematics description of the system and the cohesive elements regulating the failure at the element interfaces have been able to capture oscillating and branched patterns.

ii) The computational cost of a large number of analysis has imposed a limit on the adopted mesh size; despite of that the crack grows trying to respect the symmetry respect to the vertical central axis, while following non-trivial paths.

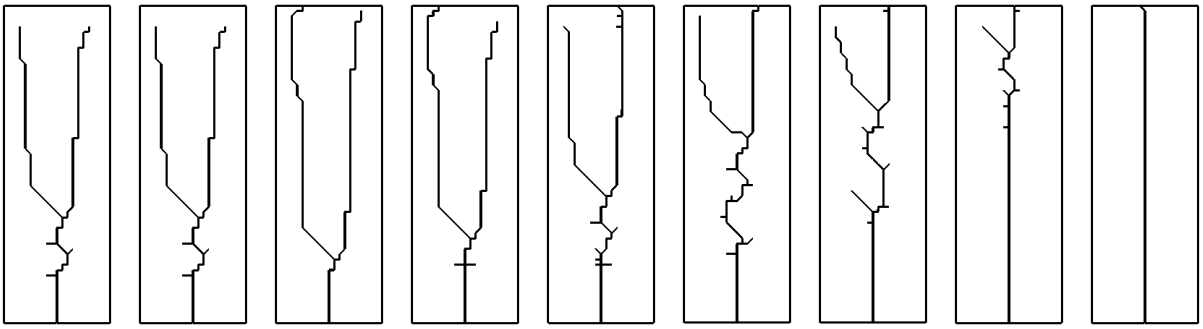

(a)	(b)	(c)	(d)	(e)	(f)	(g)	(h)	(i)
0.0001	0.00025	0.0005	0.00075	0.001	0.0025	0.005	0.0075	0.01

Figure 4-2: Fracture patterns resulting from $\Delta\vartheta = 350\,^{\circ}\mathrm{C}$. In correspondence of each figure the caption expresses the velocity in mms^{-1}.

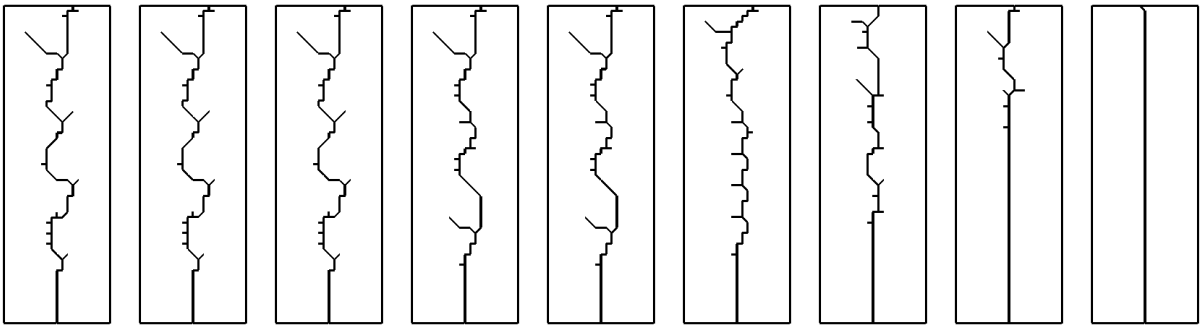

(a)	(b)	(c)	(d)	(e)	(f)	(g)	(h)	(i)
0.0001	0.00025	0.0005	0.00075	0.001	0.0025	0.005	0.0075	0.01

Figure 4-3: Fracture patterns resulting from $\Delta\vartheta = 300\,^{\circ}\mathrm{C}$. In correspondence of each figure the caption expresses the velocity in mms^{-1}.

iii) In Fig.4-2 the fracture patters are characterized by higher instability, most of them showing an initial oscillating path. Later the fracture splits into two branches, which propagate in almost straight and symmetrical directions. This results correspond to the expectations: for $\Delta\vartheta = 350\,^{\circ}\mathrm{C}$ the plate undergoes more severe temperature curvature, so higher stresses arise from incompatible deformations as well as a larger quantity of elastic energy is stored.

iv) Confirming experimental observation, for a fixed velocity, the wave length in the oscillation increases with the temperature gap. In Fig.4-5 the waves are affected by the mesh size, they tend to be small but over the limit imposed by the domain

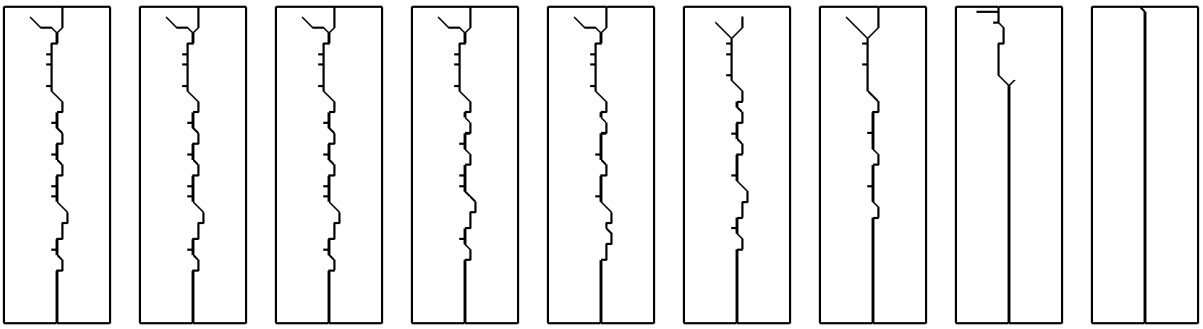

(a)	**(b)**	**(c)**	**(d)**	**(e)**	**(f)**	**(g)**	**(h)**	**(i)**
0.0001	0.00025	0.0005	0.00075	0.001	0.0025	0.005	0.0075	0.01

Figure 4-4: Fracture patterns resulting from $\Delta\vartheta = 250\,^{\circ}\mathrm{C}$. In correspondence of each figure the caption expresses the velocity in mms^{-1}.

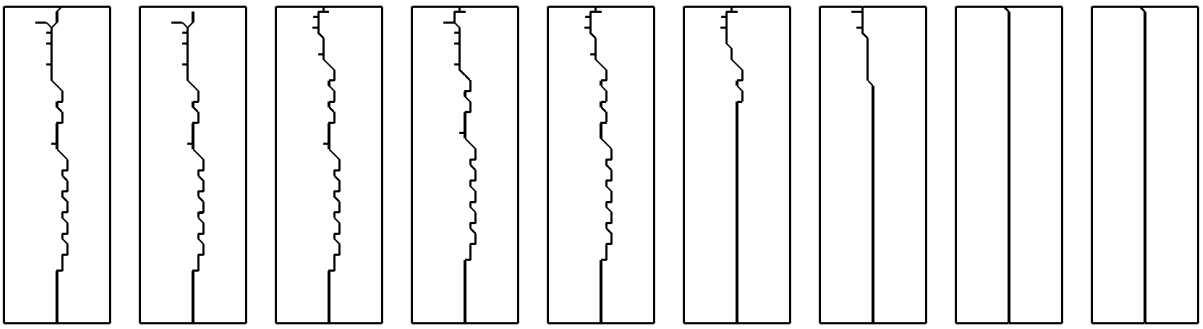

(a)	**(b)**	**(c)**	**(d)**	**(e)**	**(f)**	**(g)**	**(h)**	**(i)**
0.0001	0.00025	0.0005	0.00075	0.001	0.0025	0.005	0.0075	0.01

Figure 4-5: Fracture patterns resulting from $\Delta\vartheta = 200\,^{\circ}\mathrm{C}$. In correspondence of each figure the caption expresses the velocity in mms^{-1}.

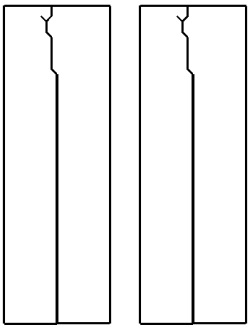

(a)	**(b)**
0.0001	0.0005

Figure 4-6: Fracture patterns resulting from $\Delta\vartheta = 150\,^{\circ}\mathrm{C}$. In correspondence of each figure the caption expresses the velocity in mms^{-1}.

discretization. In Fig.4-4 and above all Fig.4-3 the wave-length becomes larger and larger. In the latter the mesh size still affects the path-shape, but with minor relevance on the amplitude of the oscillation.

v) The incomplete set of simulations performed with $\Delta\vartheta = 150\,^{\circ}\mathrm{C}$ are mostly characterized by straight crack propagation, revealing important information about the localization of the stability threshold. The identification of limit of transition from straight to oscillating patterns is a topic of high interest for the prosecution of the present work.

4.2.1 Fracture propagation conditioned by mesh dependency.

For a fixed $\Delta\vartheta$, some of the obtained crack patterns show no changes by increasing the velocity within a certain range. This effect is due to the restriction imposed by the adopted discretization on the available fracture paths: the solution space is no rich enough to allow alternative propagations in presence of small variations of the loading conditions. For investigating this issue we performed the same analysis of Fig.4-4 but using a mesh size one half of the previous one. The results collected in Fig.4-7 clearly show how, enriching the solution space, the fracture path tends to converge to the physical one, as well as the quantity of energy dissipated.

4.2.2 Crack morphology dependence on the immersion velocity.

For a constant temperature jump $\Delta\vartheta$ we analyze the evolution of the fracture patterns with the descent velocity. For velocities lower then $10-1\mathrm{mms}^{-1}$ we observe a constance in the crack morphology, revealing a minor dependence of the propagation pattern on V. When the velocity approaches the value of $10-1\mathrm{mms}^{-1}$, or equivalently when the Peclet number tends to 1, the trend changes toward an increasing regularity in the crack path with V. We may interpret this results by comparing them with the data available in literature. In [43], [44], (see Fig.1-4) we may focus on the threshold lines between different crack morphologies. They are characterized

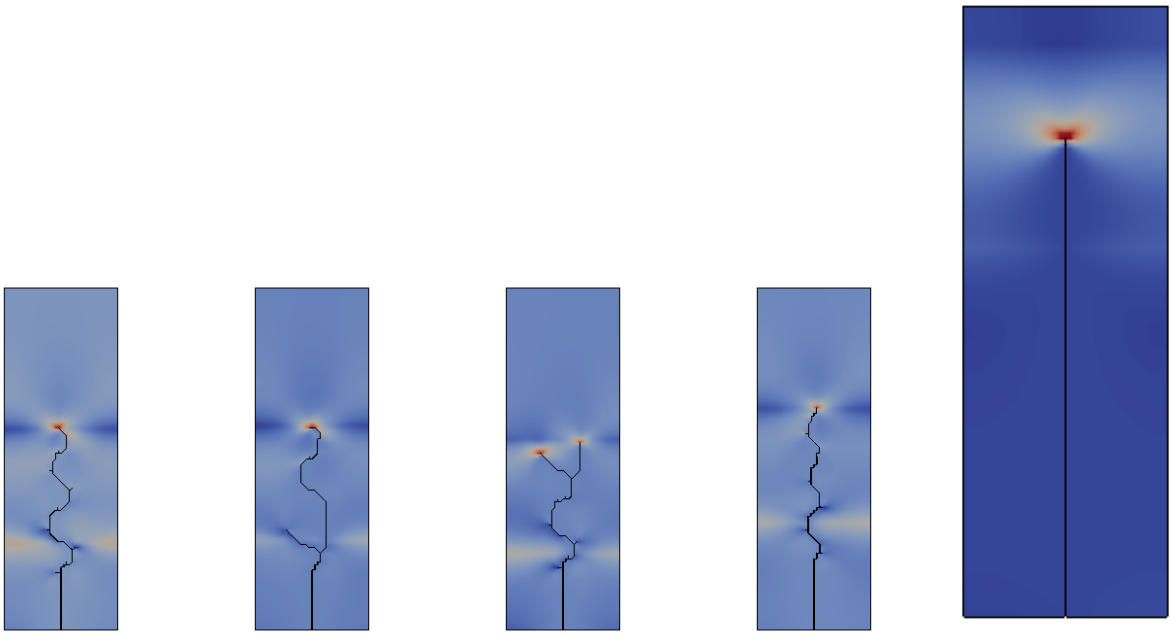

(a) 0.0001mms^{-1} **(b)** 0.00025mms^{-1} **(c)** 0.0005mms^{-1} **(d)** 0.001mms^{-1} **(e)** 0.005mms^{-1}

Figure 4-7: Fracture patterns resulting from $\Delta\vartheta = 250\,^{\circ}\text{C}$

by a fast increasing of regularity, followed by a milder trend to irregularity. The range of our velocities and the value of $\Delta\vartheta$ chosen in our experiments collocate our results in the left-top part of the graph, where in Fig.1-4 it is essentially recorded oscillating and branched patterns, without a clear distinction between them. Close to the transition threshold the same authors report the possibility of combination and transition between the two patterns. In [32], [33], Fig.4-8 an interval of lower immersion speed is considered $0.01 - 10\,\text{mms}^{-1}$. The data are collected considering the velocity versus the plate width. For V of orders $10^{-2} - 10^{-1}\,\text{mms}^{-1}$ a steady thermal regime is established. The dependence on the velocity is negligible as long as the thermal length d_{th} is greater than the distance H between cold and hot baths. At higher velocities the localization process results in decreasing the critical widths with V, as long as d_{th} remains larger than one half of the sample thickness. Under such conditions the assumption of a steady thermal profile does not hold anymore and in the numerical experiments it becomes necessary to perform a thermal analysis before solving the mechanical problem, even if the system of thermo-mechanical equations

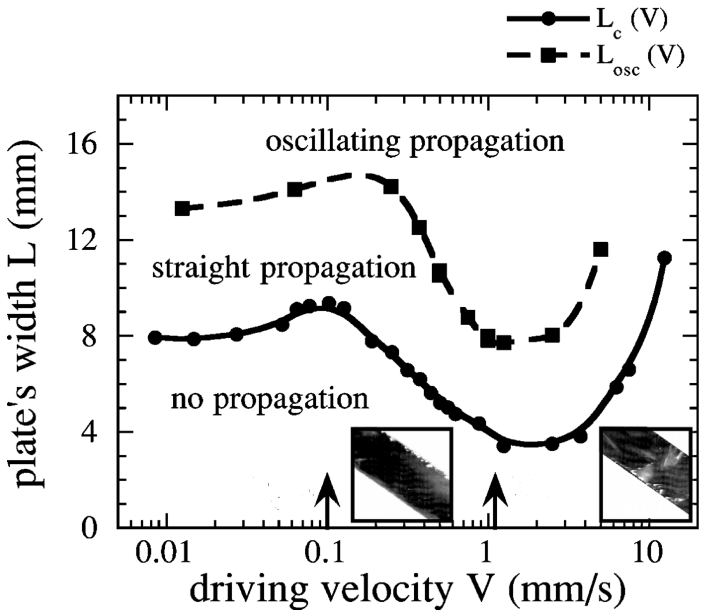

Figure 4-8: Experimental results of [34] relate the crack morphology to the plate width and the driving velocity V. The treshold lines reflect the variation of the thermal field with the V. The transition lines are controlled by (a) the distance H between the reservoirs at low velocities; (b) the thermal diffusion lenght d_{th} in the decreasing part of the graph; (c) the thickness of the plate for higher velocities, leading to a three-dimensional fracture problem and a non-smooth crack surface.

is still uncoupled. Although the finite element code is equipped with a solver for the conductive process, we focused this investigation on the lower velocity regime, to verify the adequacy of our simplest model to capture crack pattern instabilities. This assumption leave open opportunities for improvements.

Even if we are varying the temperature gap, instead of the plate width W, the outcomes of our analysis may be compared by recourse to the dimensionless parameters introduced in the section (1.3.1). In the computation of τ the two variables (W and $\Delta\vartheta$) play the same role, with different weight.

We plot in Fig.4-9 the same results of Fig.4-1 but in terms of the Peclet number and τ, whose expression we recall here

$$\tau = \frac{E^2(\alpha\Delta\vartheta)^2 W}{G_c} \tag{4.2}$$

We can observe as the extension of our data is contained within the limit of $V = \kappa/H$, which corresponds to $Pe = 1$, since the validity of our model, with steady temperature

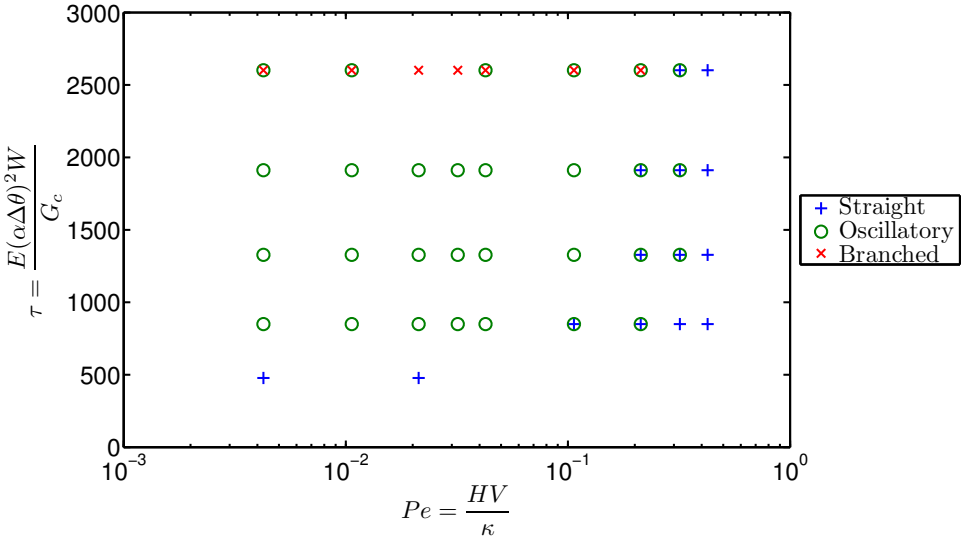

Figure 4-9: Phase Field of the crack morphology, depending on the dimensionless parameters: Pe and τ. The value $Pe = 1$ represents the limit of validity of the steady thermal state assumption.

profile imposed on the nodes, is restricted by the condition $Pe < 1$. In Fig.4-9, as well as in Fig.4-8, we observe crack patterns almost independent of of the velocity increments, as long as V does not get close the value of κ/H. The curves in Fig.4-8 shows a bump in correspondence of $V = \kappa/H$, which means an increment in the fracture regularity, before establishing an opposite trend where increments in the velocity contribute to destabilize the crack propagation. We can deduce that the numerical results so far obtained are in good agreement with the experimental ones available in literature.

4.2.3 Crack pattern depending on the plate width.

Referring to samples of thickness of the order of 10^{-1} mm, the two relevant geometric dimensions are the plate length L and width W. The importance of the role played by the latter has been observed in many experiments. The strain energy stored into the material, in function of the largeness of the plate, influences the fracture propagation as driving force.

We have chosen to investigate this aspect not varying the dimension W (so the

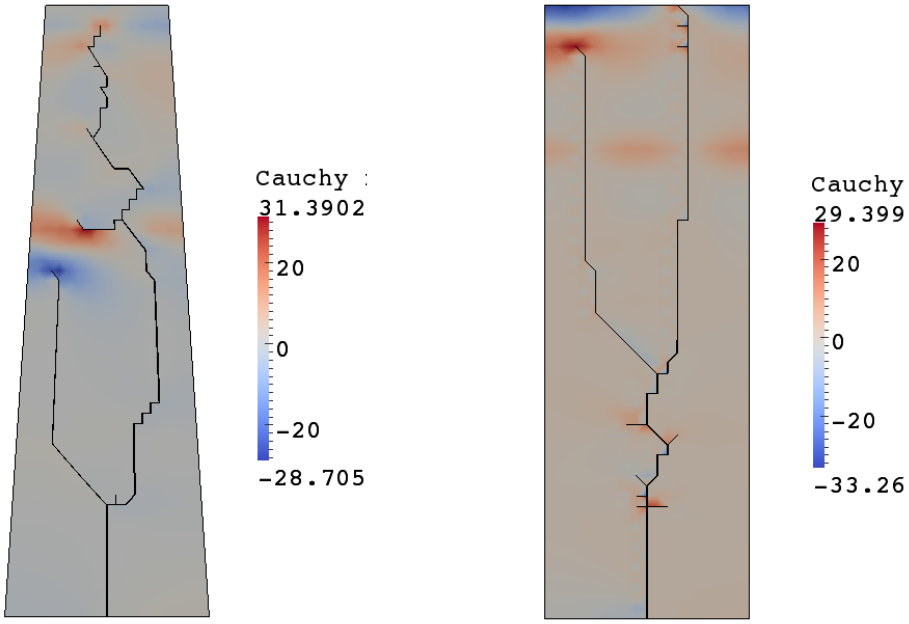

(a) Tapered plate. **(b)** Rectangular plate.

Figure 4-10: Fracture patterns resulting from $\Delta\vartheta = 350\,°\text{C}$ and $V = 0.001\text{mms}^{-1}$ (Cauchy stress units: N/mm^2).

aspect ratio of the sample) among a certain number of experiments but performing only a few analysis with tapered plates and examining the influence of a reducing width on the pattern evolution. Of particular interest is the comparison of the results with the ones obtained with a rectangular plate in the same experimental conditions. In figure Fig.4-10a we can notice how at the bottom the growth of the fracture is similar to the one in Fig.4-10b, even if the branch appears first in the tapered plate than in the rectangular one. The decreasing of W implies a reduction of the energy available to the system for feeding dissipative phenomena, in this case it means a progressive regularization of the fracture propagation. When the limit of energy for propagating two branches is reached, one of the cracks stops, while the one still active evolves and kinks, disposing of extra energy to release. The path of the second crack spontaneously tends to restore the symmetry, moving rapidly towards the center of the plate and growing with damped oscillations. The second example illustrates what happen to a crack growing with large oscillation when the section of the specimen tends to reduce. We observe in Fig.4-11 how the oscillating pattern

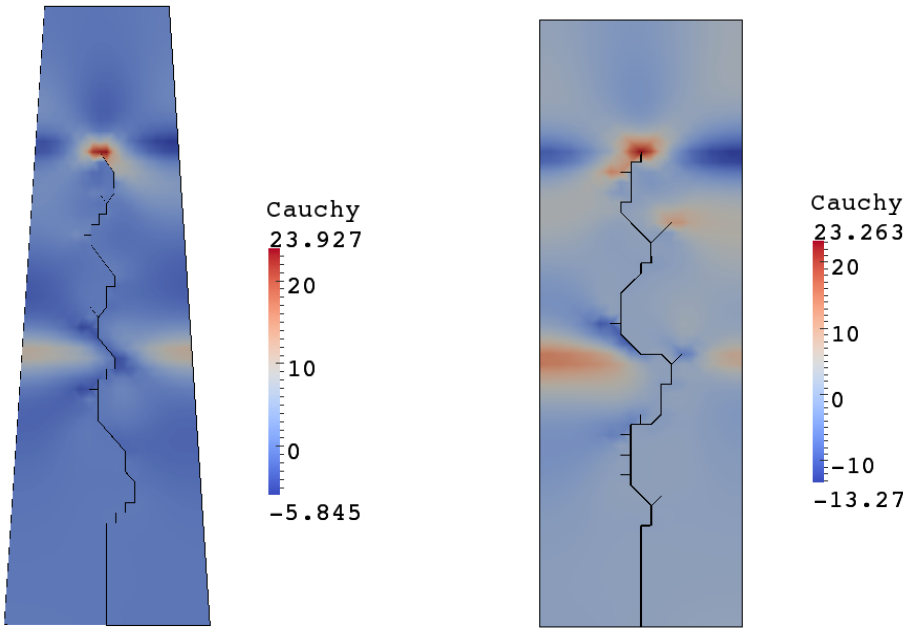

(a) Tapered plate **(b)** Rectangular plate

Figure 4-11: Fracture patterns resulting from $\Delta\vartheta = 300\,^{\circ}\mathrm{C}$ and $V = 0.0001\mathrm{mms}^{-1}$ (Cauchy stress units: $\mathrm{N/mm}^2$).

assume a sinusoidal shape and is damped by the effect of the lateral edge.

4.3 Considerations about crack tip position and energy dissipation in the fracture process.

The fracture travels along the plate, while its tip assume a certain position respect to the water surface. The localization of the crack tip can be included among the parameters governing the problem.

In [33] the authors have studied the equilibrium tip position y_{tip} as a function of the plate width W for a fixed temperature field ($\Delta\vartheta$, H and V fixed). The threshold W_c is related to the minimal amount of energy required for crack propagation. For larger width, i.e., inside the straight propagation region $W_c < W < W_{osc}$, the system adapts to the excess of available elastic energy through the crack tip position y_{tip}. For $W > W_c$, the available elastic energy is greater than the quantity needed for propagation, the crack tip position stabilizes near the hot bath, i.e., in a lower stressed

region. As the width decreases toward W_c , the available energy decreases, and the tip position moves closer to the cold bath, in a higher stressed region. Finally, when W reaches its critical value W_c , the propagation stops and the tip falls into the cold bath. Having fixed W L above its critical W_c , the crack tip position depends on the driving velocity and approximately follows the evolution of the thermal field with V. It is difficult to detect the eventuality that the crack arrests and speeds up even if its average velocity is approximately constant. The appearance of instabilities may be characterized by a propagation discontinuous in time, with a possible high value of the instantaneous velocity at the moment of kinking or branching.

Our model would require an higher mesh refinement to be able to discern this aspect in detail, although we can extract some informations by comparing the plots of the relative crack velocity $\dot{a}_{rel}$ of a straight, oscillating or branched pattern. In Fig.4-12b the relative crack velocity is very close to the unity. In the straight propagation the tip moves ahead of the water bath following the driving velocity. When the fracture oscillates, the velocity of propagation increase with the wave amplitude (see Fig.4-13b, Fig.4-14b) until becoming twice the speed of immersion in the branched configuration of Fig.4-15b.

Analyzing the growth of the parameter τ respect to the dimensionless time t_{nm}, we focus in particular on the slop of the graph represented by the expression

$$\frac{\Delta\tau}{\Delta t_{nm}} = \frac{G_c \dot{a}}{E(\alpha\Delta\vartheta)^2 WV}. \tag{4.3}$$

The comparison of the value of $\dfrac{\Delta\tau}{\Delta t_{nm}}$ for the main crack patterns confirm that the stable behavior corresponds to a minimum for the energy of the system. The values of $\dfrac{\Delta\tau}{\Delta t_{nm}}$ obtained for the straight fracture (see Fig.4-12c) are, in fact, the largest ones. The periodically stable configuration, represented by the cracks with oscillating morphology, is characterized by values of $\dfrac{\Delta\tau}{\Delta t_{nm}}$ decreasing with the wave amplitude (see Fig.4-13c, Fig.4-14c). Finally the property of instability of the branched patterns is supported by verifying the values of the slope of τ being the lowest ones among the tested cases (Fig.4-15b).

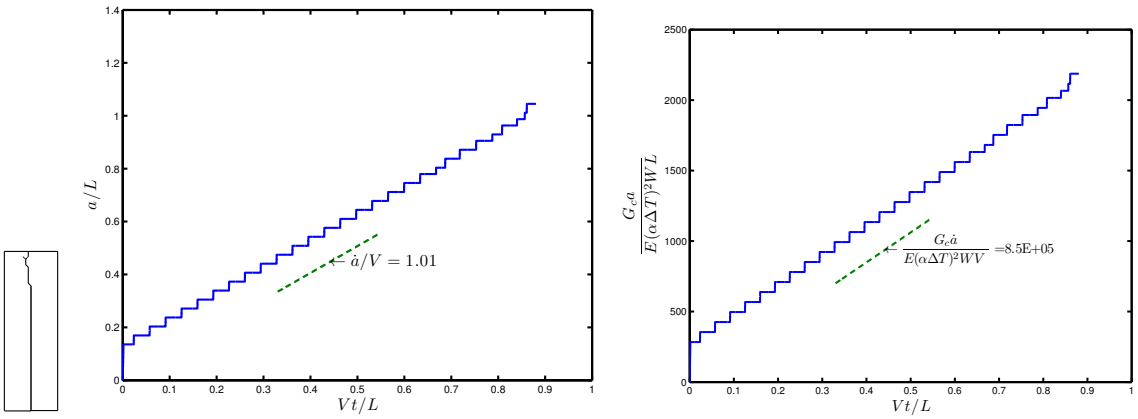

(a) **(b)** **(c)**

Figure 4-12: $\Delta\vartheta = 150\,^{\circ}\mathrm{C}$, $V = 0.0001mm/s$

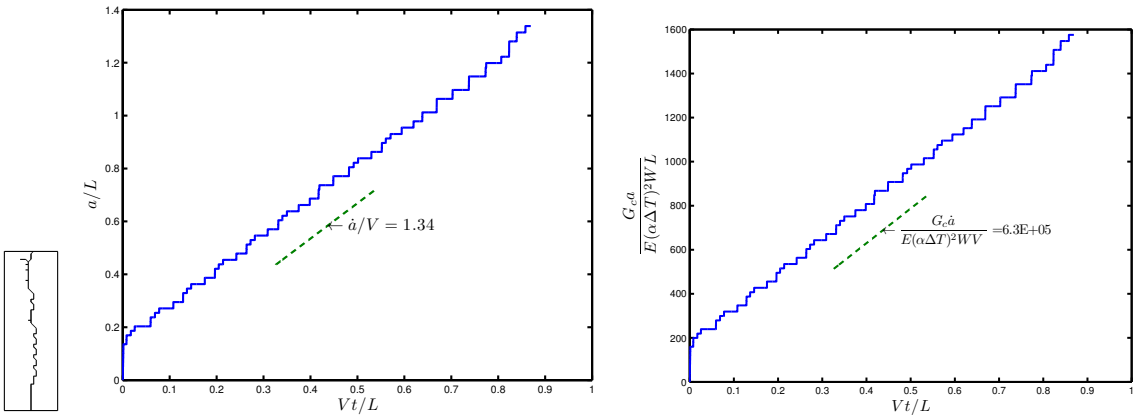

(a) **(b)** **(c)**

Figure 4-13: $\Delta\vartheta = 200\,^{\circ}\mathrm{C}$, $V = 0.0001\mathrm{mms}^{-1}$

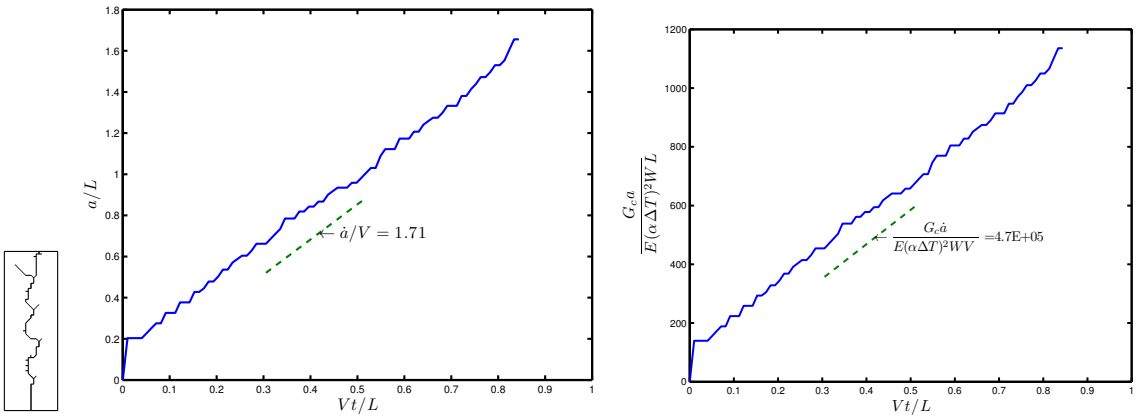

(a) **(b)** **(c)**

Figure 4-14: $\Delta\vartheta = 300\,^{\circ}\mathrm{C}$, $V = 0.0001\mathrm{mms}^{-1}$

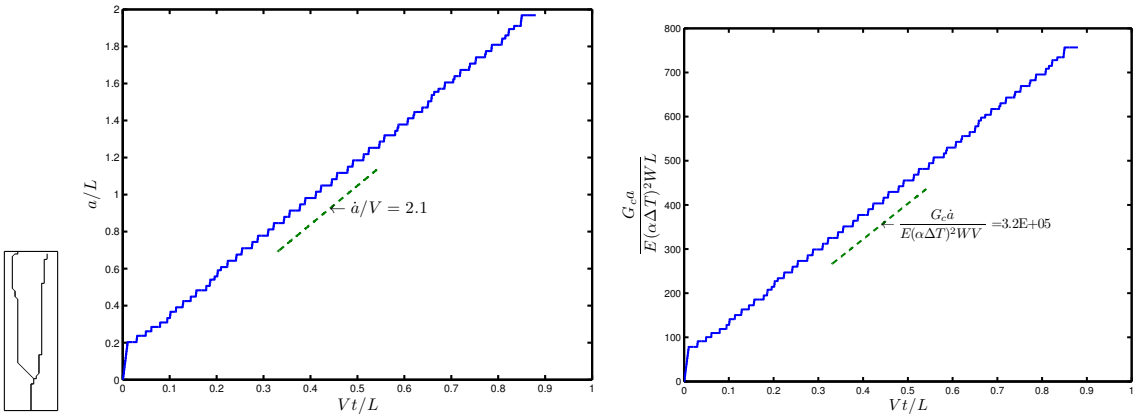

(a) **(b)** **(c)**

Figure 4-15: $\Delta\vartheta = 350\,^{\circ}\mathrm{C}$, $V = 0.0005mm/s$

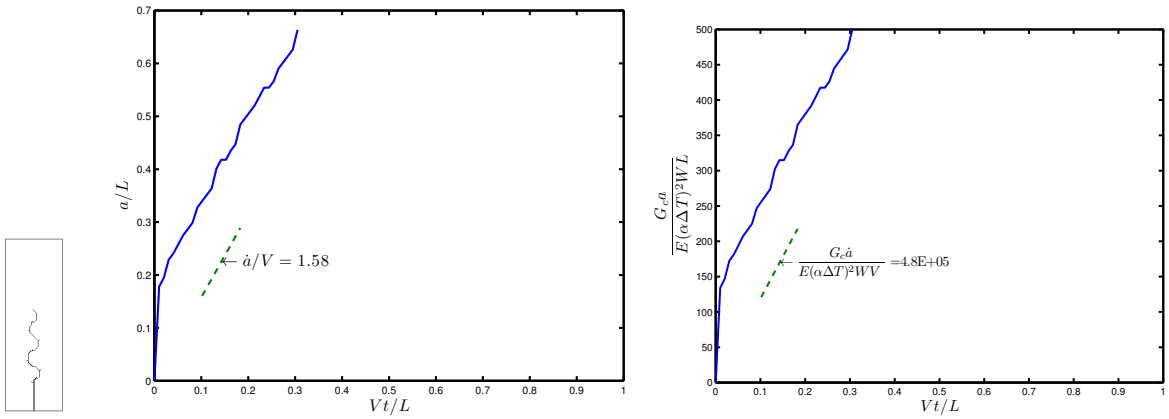

(a) **(b)** **(c)**

Figure 4-16: $\Delta\vartheta = 250\,^{\circ}\mathrm{C}$, $V = 0.0001\mathrm{mms}^{-1}$, refined mesh

Within the set of results obtained imposing the temperature jump we can deduce a trend both for the relative crack velocity and for the rate of τ. For example assuming $\Delta\vartheta = 250\,^{\circ}\mathrm{C}$ and adopting a finer mesh the relative velocity of propagation increase with the immersion velocity (compare Fig.4-16b, Fig.4-17b and.4-18b). At the same time the value of $\dfrac{\Delta\tau}{\Delta t_{nm}}$ grows with V (compare Fig.4-16c, Fig.4-17c and.4-18c) which means an increasing of the stability in the propagation. This results are confirmed by the progressive regularization of the fracture pattern observed in the simulations.

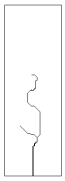

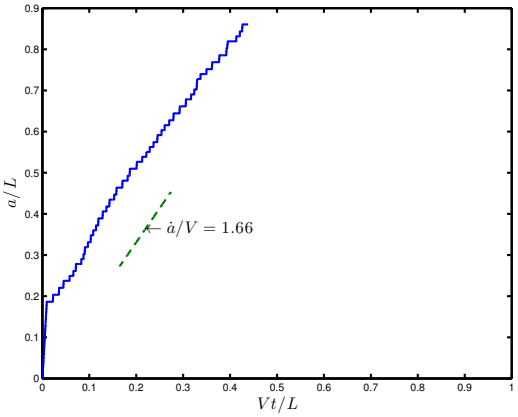

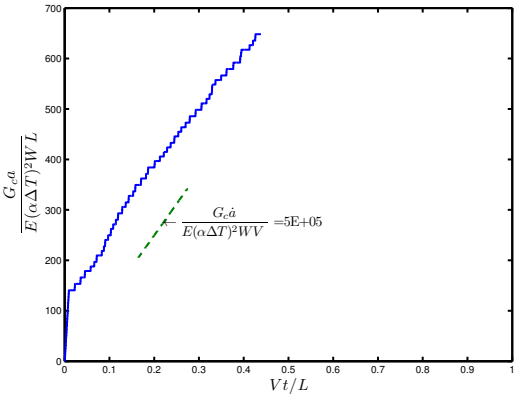

(a) **(b)** **(c)**

Figure 4-17: $\Delta\vartheta = 250\,^{\circ}\mathrm{C}$, $V = 0.00025\mathrm{mms}^{-1}$, refined mesh

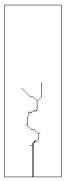

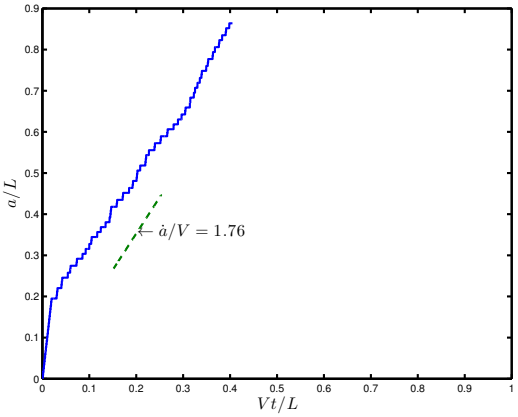

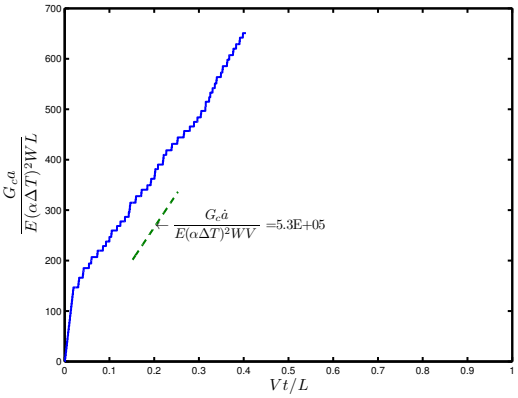

(a) **(b)** **(c)**

Figure 4-18: $\Delta\vartheta = 250\,^{\circ}\mathrm{C}$, $V = 0.0005\mathrm{mms}^{-1}$, refined mesh

4.4 Analytical consideration on the instability manifested in the crack propagation

The theory of bifurcation problems offers a framework to understand the peculiar instability associated with a quasi-static crack propagation.

The phenomena experimentally observed can be interpreted as an *Hopf bifurcation* of the solution of the equation of motion of the crack tip [36], [16], [24].

The term *bifurcation* was originally used by Poincaré to describe the "splitting" of the equilibrium solutions in a family of differential equations. Given a system of differential equations

$$\dot{\mathbf{x}} = f_\mu(\mathbf{x})\mathbf{x} \in \mathbb{R}^n, \mathbb{R}^k \tag{4.4}$$

depending on the k-dimensional parameter $\boldsymbol{\mu}$, the equilibrium solutions are obtained by solving the equation

$$f_{\boldsymbol{\mu}}(\mathbf{x}) = 0 \tag{4.5}$$

As $\boldsymbol{\mu}$ varies these equilibria are described by smooth functions of $\boldsymbol{\mu}$ away from the points $(\mathbf{x}_0, \boldsymbol{\mu}_0)$ where the Jacobian derivative of $f_{\boldsymbol{\mu}}(\mathbf{x})$ with respect to $\mathbf{x}$ $D_x f_{\boldsymbol{\mu}}(\mathbf{x})$ has a zero eigenvalue. The graph of each of these functions is a branch of equilibria, converging at the point of bifurcation $(\mathbf{x}_0, \boldsymbol{\mu}_0)$.

The *Hopf bifurcation* refers to the development of periodic orbits ("self-oscillations") from a stable fixed point, as a parameter crosses a critical value. The mathematical concept can be illustrated in a simple physical problem.

Consider the example of a rigid hoop hanging from the ceiling and a small ball rests in the bottom (see Fig.4-19). The hoop rotates with frequency ω about a vertical axis through its center For small values of ω, the ball stays at the bottom of the hoop and that position is stable. However, when ω reaches some critical value ω_0 , the ball rolls up the side of the hoop to a new position $y(\omega)$, which is stable. The ball may roll to the left or to the right, depending to which side of the vertical axis it was initially leaning. The original stable fixed point, unique solution of the differential equations

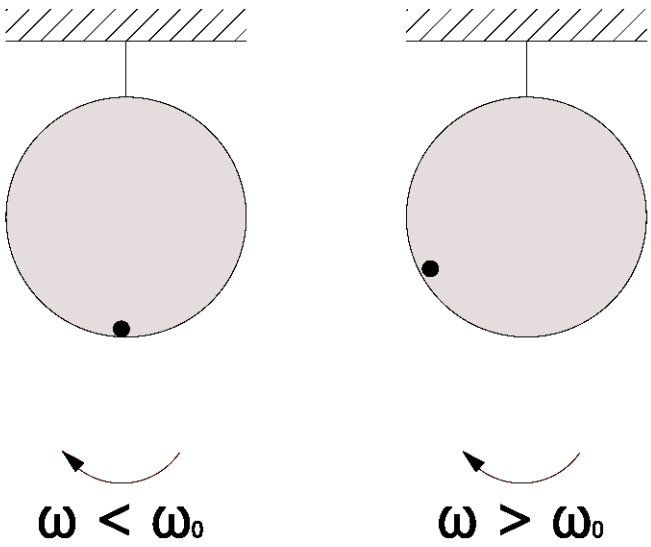

Figure 4-19: Simple experiment of a hoop rotating about its vertical axis. The position occupied by the ball depends on the angular velocity of the rotation. When a critical value w_0 is reached, the configuration with the ball at the bottom of the hoop becomes unstable.

governing the ball's motion, becomes unstable for $\omega > \omega_0$ and splits into two stable fixed points. For each $\omega > \omega_0$ there is a stable, invariant circle of fixed points due to the symmetries present in the problem.

In this example of a physical problem depending on a parameter, the angular velocity the character of the solution changes abruptly and ω_0 can be classified as a Hopf bifurcation point. The appearance of the stable closed orbits is interpreted as a "shift of stability" from the original stationary solution to the periodic one.

Let us try to express the similarity between this example and the fracture problem we are interested in. The drastic change in the crack morphology according to the experimental parameters is a clear manifestation of an instability phenomenon. Furthermore the arising of periodic stable solutions is evident in the oscillating patterns characterized by wavelength and amplitude depending on the test settings ($\Delta\vartheta$, V, W, H). The solution is conditioned by the symmetry of the problem, however, also in this case, the first deviation from the straight direction to the left or to the right is due to local asymmetries (material defects in the physical reality, perturbations of

the solution in the numerical one).

It is possible to identify another threshold, which represents the limit of stability for the oscillating crack pattern and the appearance of branching. It delimits the transient from periodically stable to unstable solutions.

Let us formalize the definition of a Hopf bifurcation point [24].

Suppose that the system

$$\dot{\mathbf{x}} = f_\mu(\mathbf{x}) \qquad\qquad \mathbf{x} \in \mathbb{R}^n, \quad \mu \in \mathbb{R} \tag{4.6}$$

has an equilibrium point (x_0, μ_0) at which the following properties are satisfied:

i) $D_x f_{\mu_0}(\mathbf{x_0})$ has a simple pair of pure imaginary eigenvalues $\lambda(\mu)$, $\overline{\lambda(\mu)}$ and no other eigenvalues with zero real parts;

ii) $\lambda(\mu)$, $\overline{\lambda(\mu)}$ vary smoothly with μ along the curve of equilibria $(\mathbf{x}(\mu), \mu)$ with the property: $\dfrac{d}{d\mu}\left(Re\lambda(\mu)\right)|_{\mu=\mu_0} \neq 0$

Under the above conditions there exist continuous functions $\mu = \mu(\epsilon)$ and $T = T(\epsilon)$, depending on a parameter ϵ, with

$$\mu(0) = \mu_0 \tag{4.7}$$

$$T(0) = 2\pi\beta^{-1} \qquad\qquad \lambda(\mu), \overline{\lambda(\mu)} = \pm i\beta \tag{4.8}$$

such that there are non-constant periodic solutions $\mathbf{x}(t, \epsilon)$ with period $T(\epsilon)$ which collapse into $\mathbf{x}_0$ as $\epsilon \to 0$.

In [36] the authors analyze the variety of crack patterns object of this study by the point of view of the theory of instability. They investigate the motion of the crack tip as solution of the two basic equation describing quasi-static crack propagation

$$K_I = K_{Ic} \tag{4.9}$$

$$K_{II} = 0 \tag{4.10}$$

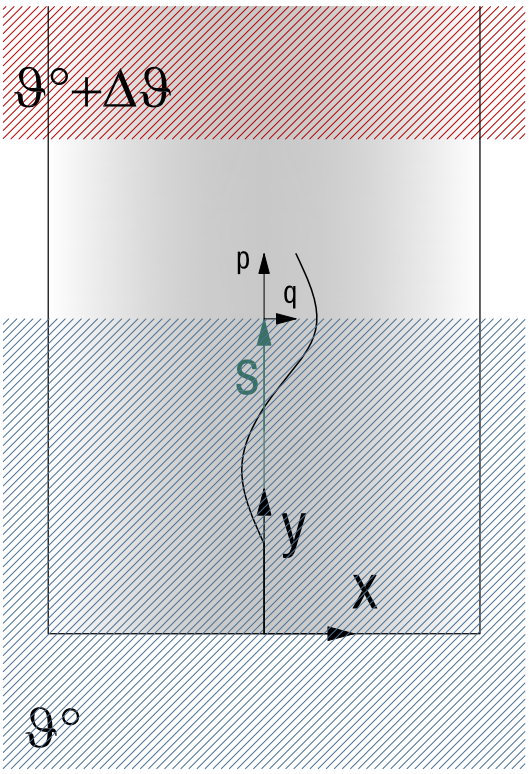

Figure 4-20: Reference system for the description of the crack tip position respect to the water bath surface, denoted by the parameter s.

The position of the crack tip correspond to the point where the stress intensity factor in mode I is equivalent to its critical value and a negative K_I increment for infinitesimal crack extension. The second necessary condition is obtained assuming the principle of local symmetry, which corresponds to a criterion of propagation of the crack toward the direction where the shear stress vanishes.

The two equation problem has been posed adopting the hypothesis of infinite plate width and reformulating it as a linearized eigenvalue problem. The Central Manifold theorem guarantees that the character of the solution can be detected studying the linear approximation of the equation, in a suitable neighborhood of the bifurcation point.

The crack tip position has been described by two coordinates $(q(s), p(s))$ respect to a reference system located at the water bath surface, marked by the variable s (see

Fig.4-20). The straight propagation,in particular, is obtained when $p(s) = 0$ holds along all the plate. To establish the limit of stability of this solution they consider the eigenvalue with the largest real part z^* (in absolute value), assuming to look at the long term behavior of the fracture (when the parameter s tends to infinity). The sign of $Re(z^*)$ changes accordingly with the experimental data. Of particular interest is the point, in the data space, corresponding to a null value of $Re(z^*)$, because it represents the point of bifurcation of the solution, so the passage from the stable straight solution ($Re(z^*) < 0$) to the instable one ($Re(z^*) > 0$). The Hopf bifurcation point is characterize by a pair of pure imaginary eigenvalues ($z^* = \pm i\beta$) and the wavelength of the oscillating pattern is function of β.

Chapter 5

Conclusion

5.1 Current development

There are fundamental limits to the processing power of a single processor and in general high resolution requires lots of memory and large computational effort. To overcome this obstacle it is possible to distribute work and data among multiple processors appropriately programming the sequence of instructions and the data subdivision. SIMD (single instruction, multiple data) and MIMD (multiple instruction, multiple data) are the traditional models for parallel machines. The memory organization can be private, for each processor, or shared. Shared memory permits to parallelize serial program gradually, while distributed memory requires partitioning and distributing both data and work across processors, with an initial larger effort but with the advantage of an higher scalability.

A multi-thread version of our code, working on shared memory is already implemented and it has been largely used for reducing the cost of our simulations.

We are currently working on a parallel implementation of the finite element code adopting MPI (Message-Passing Interface), which is a *message-passing library interface specification* base on private memory distribution.

MPI allows overlap of computation and communication, in the sense that the computational effort is (preferably equally) distributed among all the processors and the exchange of data happens through cooperative operations on each process.

MPI is not and independent language: all MPI operations are expressed as functions, subroutines, or methods, according to the appropriate language bindings, which for C, C++, Fortran-77, and Fortran-95, are part of the MPI standard. The standard has been defined through an open process by a community of parallel computing vendors, computer scientists, and application developers. The main advantage of establishing a message-passing standard is portability.

To design parallel algorithms it is necessary to identify the part of the problem that can be parallelized and decompose them into tasks. A crucial aspect consists of determining the necessary communication patterns among tasks assigned to different processors.

A good programming strategy try to maximize the work that can be done in parallel, balancing the load so that it remains evenly divided along the execution. It is important to possibly reduce the work not present in the equivalent serial computation: process startup and shutdown costs, communication, synchronization, redundancy and speculative work.

In the parallel code under development the distribution of data is base on domain decomposition. Each processor is delegated to perform the thermo-mechanical analysis and any topological change concerning a specific sub-domain of the whole body. The information about forces applied on nodes shared among multiple processors is exchanged through a suitable communication schema.

The implementation includes a re-formulation of the two-dimensional fragmentation code, able to manage the fracture propagation within each process as well as the crossing of sub-domain boundaries and the insertion of cohesive elements along sub-domain interfaces.

The efficiency of the parallel implementation requires minimizing the number of messages exchanged, by reducing the inter-dependency among processors.

The code has been conceived so that it can run sequentially or in parallel, on clusters with shared or separate memory.

5.2 Possible Further Developments

An immediate and natural continuation of this research may consist of including higher immersion velocities by solving the fully coupled thermo-mechanical problem.

A first investigation of the mesh dependence issue can be carried out by introducing randomness and increasing resolution once we dispose of the complete parallel implementation of the code. A deeper analysis of the directionality bias may involve the study of nonlocal variational fracture methods.

We refer to generalizations of Griffith's theory proposed in literature to determine the crack path based on energy criteria. In particular on the subject of brittle fracture several contributions produced in the area of calculus of variation have the attention mainly focused on the application of *free discontinuity models* to the prediction of fracture. Free discontinuity models deal with the minimization of energy functionals composed of bulk and surface terms, which admit the crack path as a primary unknown. The displacement field $\mathbf{u}$ and its discontinuity set of J_u (representing fracture) are the arguments of an energy functional $E(\mathbf{u}, J_u)$ composed of bulk potential energy and a surface (or interface) parts. The latter represents the energy dissipated during the nucleation and propagation of fractures within the body. Optimal solutions $(\mathbf{u}, J_u)$ are sought through a time-continuous minimization process. The original model in [12] dealing with a global minimization problem, has been followed by variants considering local minimization [8]. Concerning numerical approximations: strong approaches explicitly account for discontinuities and consider finite element models incorporating discontinuous test functions and mesh adaptivity [26]; weak approaches model fracture through an auxiliary damage variable and introduce energy approximation by means of families of elliptic functionals [3]. In both cases, convergence behavior of discrete approximations has been proved, using arguments of the Γ-convergence theory [7].

Their distinctive feature, as compared to stress based crack path tracking strategies, consists of the fully variational formulation of the fracture problem, both in terms of the displacement field and crack pattern. In [25] it has been demonstrated

that the convergence of free discontinuity procedures requires the adoption of very fine fixed meshes and/or adaptive triangulations, in order to avoid mesh-dependence of the crack predictions [13]. Adaptive models involve aspects of configuration and mechanics, which compete against each other to determine the minimal energy solution in terms of nodal displacements, mesh geometry, and crack pattern. [39] They may represent a rigorous approach to the mesh dependency issue, which remains open in this work, as a stimulus for future research.

Appendix A

Properties and invariants of kinematic variables

A.0.1 Index notation

So far the algebra of vector and tensor has been presented in symbolic (or direct) notation but in computational mechanics it is essential to refer vectorial (and tensorial) quantities to a basis. In order to introduce component expressions relative to a right handed orthonormal tridimensional euclidean space we consider a set of basis vectors $\mathbf{e_1}, \mathbf{e_2}, \mathbf{e_3}$ with the property of being orthonormal. Then any vector $\mathbf{v}$ and any tensor $\mathbf{A}$ are uniquely represented by a linear combination of, rispectively, the basis vectors or their diadic products:

$$\mathbf{v} = v_1\mathbf{e_1} + v_2\mathbf{e_2} + v_3\mathbf{e_3} = v_a\mathbf{e_a} \qquad a = 1, 2, 3 \tag{A.1}$$

$$\mathbf{A} = A_{ij}\,\mathbf{e}_i \otimes \mathbf{e}_j \tag{A.2}$$

where the Einstein summation convention has been adopted. We label $X_A, A = 1, 2, 3$, as the material (or referential) coordinates of the position vector $\mathbf{X}$ and $x_a, a = 1, 2, 3$, as the spatial (or current) coordinates of the position vector $\mathbf{x}$. The deformation gradient $\mathbf{F}$ is a second order tensor which involve points in two distinct configurations

and it is therefore called two-point tensor.

$$\mathbf{F} = \frac{\partial \boldsymbol{\chi}}{\partial \mathbf{X}} = \operatorname{Grad} \mathbf{x}(\mathbf{X}, t) \qquad F_{iH} = \frac{\partial x_i}{\partial X_H} \tag{A.3}$$

$$\mathbf{F}^{-1} = \frac{\partial \boldsymbol{\chi}^{-1}}{\partial \mathbf{x}} = \operatorname{grad} \mathbf{X}(\mathbf{x}, t) \qquad F_{Hi} = \frac{\partial X_H}{\partial x_i} \tag{A.4}$$

$$\mathbf{F}\mathbf{F}^{-1} = \mathbf{I} \qquad F_{iH} F^{-1}_{Hj} = \delta_{ij} \tag{A.5}$$

$$\mathbf{F}^{-1}\mathbf{F} = \mathbf{I} \qquad F^{-1}_{Hi} F_{iK} = \delta_{HK} \tag{A.6}$$

The expression Grad and grad are adopted to distinguish between material and spatial gradient. We recall the derivatives with respect to $\mathbf{F}$ of the determinant of $\mathbf{F}$ (Jacobian)

$$\det \mathbf{F} = J \qquad \frac{\partial J}{\partial \mathbf{F}} = J\mathbf{F}^{-T} \qquad \frac{\partial J}{\partial F_{iH}} = J F^{-1}_{Hi} \tag{A.7}$$

The first invariant of the Cauchy-Green deformation tensor $\mathbf{C} = \mathbf{F}^T\mathbf{F}$; $C_{HK} = F_{iH}F_{iK}$ is defined as follow:

$$I_1 = \operatorname{tr} \mathbf{C} = \mathbf{C} : \mathbf{I} = C_{JJ} \tag{A.8}$$

and it derivative with respect to $\mathbf{C}$ and $\mathbf{F}$ are:

$$\frac{\partial I_1}{\partial \mathbf{C}} = \mathbf{I} \qquad \frac{\partial C_{JJ}}{\partial C_{HK}} = \delta_{JH}\delta_{JK} = \delta_{HK} \tag{A.9}$$

$$\frac{\partial I_1}{\partial \mathbf{F}} = 2\mathbf{F} \qquad \frac{\partial C_{JJ}}{\partial F_{jI}} = \frac{\partial C_{JJ}}{\partial C_{HK}} \frac{\partial (F_{iH}F_{iK})}{\partial F_{jI}} = 2F_{jI} \tag{A.10}$$

We recall the definition of the fourth-order identity tensors $\mathbb{I}$ and its transpost $\mathbb{I}^T$

$$(\mathbb{I})_{IJHK} = \delta_{IH}\delta_{JK} \qquad (\mathbb{I}^T)_{IJHK} = \delta_{IK}\delta_{JH} \tag{A.11}$$

We deduce the expression of the derivative of the inverse of the deformation gradient $\mathbf{F}^{-1}$ with respect to $\mathbf{F}$:

$$\frac{\partial \mathbf{F}^{-1}}{\partial \mathbf{F}} = -\mathbf{F}^{-1} \odot \mathbf{F}^{-1} \qquad \frac{\partial F^{-1}_{Hb}}{\partial F_{aK}} = -F^{-1}_{Ha} F^{-1}_{Kb} \tag{A.12}$$

where $\odot$ operator for non-symmetric tensors is:

$$\left(\mathbf{F}^{-1} \odot \mathbf{F}^{-1}\right)_{HbaK} = F^{-1}_{Ha} F^{-1}_{Kb} \tag{A.13}$$

Proof:

$$F^{-1}_{Hb} F_{bI} = \delta_{HI} \qquad \frac{\partial \left(F^{-1}_{Hb} F_{bI}\right)}{\partial F_{aK}} = \frac{\partial F^{-1}_{Hb}}{\partial F_{aK}} F_{bI} + F^{-1}_{Ha} \delta_{IK} = 0 \tag{A.14}$$

$$\frac{\partial F^{-1}_{Hb}}{\partial F_{aK}} F_{bI} F^{-1}_{Ic} = -F^{-1}_{Ha} \delta_{IK} F^{-1}_{Ic} \qquad \frac{\partial F^{-1}_{Hb}}{\partial F_{aK}} = -F^{-1}_{Ha} F^{-1}_{Kb} \tag{A.15}$$

Or, alternatively:

$$F_{aH} F^{-1}_{Hb} = \delta_{ab} \qquad \frac{\partial \left(F_{aH} F^{-1}_{Hb}\right)}{\partial F_{cK}} = \delta_{ac} F^{-1}_{Kb} + F_{aH} \frac{\partial F^{-1}_{Hb}}{\partial F_{cK}} = 0 \tag{A.16}$$

$$F^{-1}_{Ja} F_{aH} \frac{\partial F^{-1}_{Hb}}{\partial F_{cK}} = -F^{-1}_{Ja} \delta_{ac} F^{-1}_{Kb} \qquad \frac{\partial F^{-1}_{Jb}}{\partial F_{cK}} = -F^{-1}_{Jc} F^{-1}_{Kb} \tag{A.17}$$

It follows that:

$$\frac{\partial \mathbf{F}^{-T}}{\partial \mathbf{F}^{T}} = \frac{\partial \mathbf{F}^{-1}}{\partial \mathbf{F}} \tag{A.18}$$

and

$$\frac{\partial \mathbf{F}^{-T}}{\partial \mathbf{F}} = \frac{\partial \mathbf{F}^{-T}}{\partial \mathbf{F}^{T}} : \frac{\partial \mathbf{F}^{T}}{\partial \mathbf{F}} = \frac{\partial \mathbf{F}^{-1}}{\partial \mathbf{F}} : \mathbb{I}^{T} = \frac{\partial \mathbf{F}^{-1}}{\partial \mathbf{F}} \tag{A.19}$$

Bibliography

[1] G. I. Barenblatt. The mathematical theory of equilbrium of cracks in brittle fractures. *Archives of Applied Mechanics*, 7:55–129, 1962.

[2] M. A. Biot. *Variational principles in heat transfer: a unified Lagrangian analysis of dissipative phenomena.* The Clarendon press, Oxford, 1970.

[3] B. Bourdin, G. A. Francfort, and J. J. Marigo. Numerical experiments in revisited brittle fracture. *Journal of the Mechanics and Physics of Solids*, 48:797–826, 2000.

[4] G. T. Camacho and M. Ortiz. Computational modelling of impact damage in brittle materials. *International Journal of Solids and Structures*, 33:2899–2938, 1996.

[5] B. Cotterell. On brittle fracture paths. *International Journal of Fracture*, 1:96–103, 1965.

[6] B. Cotterell and J. R. Rice. Slightly curved or kinked cracks. *International Journal of Fracture*, 16:155–169, 1980.

[7] G. Dal Maso. *An Introduction to* Γ*-convergence*. Birkhäuser, Boston, 1993.

[8] G. Dal Maso and R. Toader. A model for the quasi-static growth of brittle fractures based on local minimization. 12:1773–1800, 2002.

[9] R. D. Deegan, S. Chheda, L. Patel, M. Marder, and H. L. Swinney. Wavy and rough cracks in silicon. *Physical Review E*, 67:066209–1–066209–7, 2003.

[10] D. S. Dugdale. Yielding of steel sheets containing clits. *Journal of the Mechanics and Physics of Solids*, 8:100–104, 1960.

[11] B. D. Ferney, M. R. DeVary, and K. J. Hsia. Oscillatory crack growth in glass. *Scripta Materialia*, 41:275–281, 1999.

[12] G. A. Francfort and J. J. Marigo. Revisiting brittle fracture as an energy minimization problem. *Journal of the Mechanics and Physics of Solids*, 46:1319–1342, 1998.

[13] F. Fraternali, M. Negri, and M. Ortiz. On the convergence of 3d free discontinuity models in variational fracture. *International Journal of Fracture*, 166:3–11, 2010.

[14] R. V. Goldstein and R. L. Salganik. Brittle fracture of solids with arbitrary cracks. *International Journal of Fracture*, 10:507–523, 1974.

[15] A. A. Griffith. The phenomena of rupture and flow in solids. *Phil. Trans. Roy. Soc. London*, 18:163–198, 1920.

[16] J. Guckenheimer and P. Holmes. *Nonlinear oscillations, dynamical systems, and bifurcations of vector fields.* Springer-Verlag, New York, 1983.

[17] M. E. Gurtin, E. Fried, and L. Anand. *The mechanics and thermodynamics of continua.* Cambridge University Press, New York, 2010.

[18] G. A. Holzapfel. *Nonlinear Solid Mechanics: A Continuum Approach for Engineering.* John Wiley & Sons, New York, 2000.

[19] J. R. Hughes. *The Finite Element Method: Linear Static and Dynamic Finite Element Analysis.* Dover Publications, USA, 2000.

[20] F. P. et al. Incropera. *Fundamentals of heat and mass transfer.* Wiley, Hoboken, NJ, 2007.

[21] G. R. Irwin. Analysis of stresses and strains near the end of a crack traversing a plate. *Journal of Applied Mechanics*, 24:361–364, 1957.

[22] B. Kilic and E. Madenci. Prediction of crack paths in a quenched glass plate by using peridynamic theory. *International Journal of Fracture*, 156:165–177, 2009.

[23] M. Marder. Instability of a crack in a heated strip. *Physical Review E*, 49:51–54, 1994.

[24] J. E. Marsden and M. McCracken. *The Hopf bifurcation and its applications.* Springer-Verlag, New York, 1976.

[25] M. Negri. The anisotropy introduced by the mesh in the finite element approximation of the mumford-shah functional. *Numerical Functional Analysis and Optimization*, 20:957–982, 1999.

[26] M. Negri. A discontinuous finite element approximation of free discontinuity problems. *Advances in Mathematical Sciences and Applications*, 15:283–306, 2005.

[27] D. R. Oakley and N. F. Knight. Adaptive dynamic relaxation algorithm for non-linear hyperelastic structures. *Computer Methods in Applied Mechanics and Engineering*, 126:67–129, 1995.

[28] M. Ortiz and A. Pandolfi. Finite-deformation irreversible cohesive elements for three-dimensional crack propagation analysis. *International Journal for Numerical Methods in Engineering*, 44:1267–1282, 1999.

[29] A. Pandolfi and M. Ortiz. Solid modeling aspects of three-dimensional fragmentation. *Engineering with Computers*, 14:287–308, 1998.

[30] A. Quarteroni. *Modellistica numerica per problemi differenziali.* Springer, Milano, 2003.

[31] J. R. Rice. A path-indipendent integral and the approximate analysis of strain concentration by notches and cracks. *Journal of Applied Mechanics*, 35:379–386, 1968.

[32] O. Ronsin, F. Heslot, and O. Perrin. Experimental study of quasistatic crack propagation. *Physical Review Letters*, 75:2352–2355, 1995.

[33] O. Ronsin and O. Perrin. Multi-fracture propagations in a directional crack growth experiment. *Europhysics Letters*, 38:435–440, 1997.

[34] O. Ronsin and O. Perrin. Dynamics of quasistatic directional crack growth. *Physical Review E*, 58:7878–7886, 1998.

[35] S. Salsa. *Equazioni a derivate parziali: metodi modelli applicazioni.* Springer, Milano, 2004.

[36] S. Sasa, K. Sekimoto, and H. Nakanishi. Oscillatory instability of crack propagations in quasistatic fracture. *Physical Review E*, 50:1733–1736, 1994.

[37] G. C. Sih and F. Erdogan. On the crack extension in plates under plane loading and transvers shear. *Journal of Basic Engineering*, 85:519–527, 1963.

[38] L. Stainier and M. Ortiz. Study and validation of a variational theory of thermo-mechanical coupling in finite visco-plasticity. *International Journal of Solids and Structures*, 47:705–715, 2010.

[39] P. Thoutireddy and M. Ortiz. A variational r-adaption and shape-optimization method for finite deformation elasticity. *International Journal for Numerical Methods in Engineering*, 61:1–21, 2004.

[40] C. Truesdell and W. Noll. *The Nonlinear Field Theories of Mechanics.* Springer, Berlin, 1965.

[41] P. Underwood. *Computational Methods for Transient Dynamic Analysis.* Belytschko and Hughes eds, Amsterdam, 1983.

[42] Q. Yang, L. Stainier, and M. Ortiz. A variational formulation of the coupled thermo-mechanical boundary-value problem for general dissipative solids. *Journal of the Mechanics and Physics of Solids*, 54:401–424, 2006.

[43] A. Yuse and M. Sano. Transition between crack patterns in quenced glass plates. *Letters to Nature*, 362:329–331, 1993.

[44] A. Yuse and M. Sano. Instabilities of quasi-static crack patterns in quenced glass plates. *Physica D*, 108:365–378, 1997.